

## Lidar studies of interannual, seasonal, and diurnal variations of polar mesospheric clouds at the South Pole

Xinzha Chu and Chester S. Gardner

Department of Electrical and Computer Engineering, University of Illinois at Urbana-Champaign, Urbana, Illinois, USA

Raymond G. Roble

High Altitude Observatory, National Center for Atmospheric Research, Boulder, Colorado, USA

Received 10 May 2002; revised 9 November 2002; accepted 19 December 2002; published 8 March 2003.

[1] Polar mesospheric clouds (PMC) were observed by an Fe Boltzmann temperature lidar at the South Pole in the 1999–2000 and 2000–2001 austral summer seasons. We report the study of interannual, seasonal, and diurnal variations of PMC using more than 430 h of PMC data. The most significant differences between the two seasons are that in the 2000–2001 season, the PMC mean total backscatter coefficient is 82% larger and the mean centroid altitude is 0.83 km lower than PMC in the 1999–2000 season. Clear seasonal trends in PMC altitudes were observed at the South Pole where maximum altitudes occurred around 10–20 days after summer solstice. Seasonal variations of PMC backscatter coefficient and occurrence probability show maxima around 25–40 days after summer solstice. Strong diurnal and semidiurnal variations in PMC backscatter coefficient and centroid altitude were observed at the South Pole with both in-phase and out-of-phase correlations during different years. A significant hemispheric difference in PMC altitudes was found, that the mean PMC altitude of 85.03 km at the South Pole is about 2–3 km higher than PMC in the northern hemisphere. Through comparisons with the NCAR Thermosphere-Ionosphere-Mesosphere-Electrodynamics General Circulation Model (TIME-GCM), the hemispheric difference in PMC altitude is attributed to the hemispheric differences in the altitudes of supersaturation region and in the upwelling vertical wind, which are mainly caused by different solar forcing in two hemispheres that the solar flux in January is 6% greater than the solar flux in July due to the Earth's orbital eccentricity. Gravity wave forcing also contributes to these differences.

INDEX TERMS: 0340 Atmospheric Composition and Structure: Middle atmosphere—composition and chemistry; 1650 Global Change: Solar variability; 3334 Meteorology and Atmospheric Dynamics: Middle atmosphere dynamics (0341, 0342); 3360 Meteorology and Atmospheric Dynamics: Remote sensing; 3367 Meteorology and Atmospheric Dynamics: Theoretical modeling

**Citation:** Chu, X., C. S. Gardner, and R. G. Roble, Lidar studies of interannual, seasonal, and diurnal variations of polar mesospheric clouds at the South Pole, *J. Geophys. Res.*, 108(D8), 8447, doi:10.1029/2002JD002524, 2003.

### 1. Introduction

[2] Polar mesospheric clouds (PMC) and their visual counterparts noctilucent clouds (NLC) are the thin scattering layers occurring in the mesopause region ( $\sim 85$  km) at high latitudes ( $\sim$  poleward of  $50^\circ$ ) in both hemispheres mainly during the three months surrounding summer solstices when temperatures fall below the frost point ( $\sim 150$  K). It is generally believed that PMC/NLC are composed of water ice particles, and are regarded as sensitive tracers of middle and upper atmospheric water vapor and temperatures, and possibly as an indicator of long-term global climate change [Thomas, 1991, 1994; Avaste, 1993]. The geographic coverage and occurrence frequency of NLC sightings have been increasing in the past decades. Recent-

ly, NLC have been observed at midlatitude such as Utah ( $41^\circ\text{N}$ ) [Taylor *et al.*, 2002]. This has been related to decreasing mesopause temperature and increasing mesospheric water vapor concentration possibly caused by the rising level of mesospheric  $\text{CO}_2$  and  $\text{CH}_4$ , respectively [Thomas, 1996]. The idea that PMC/NLC particles are composed of water ice was first suggested by Humphreys [1933], then later taken up by Hestvedt [1961, 1962], Chapman and Kendall [1965], Charlson [1965, 1966], Reid [1975], and Gadsden [1981]. More comprehensive models including microphysics of ice formation were developed by Turco *et al.* [1982], Jensen and Thomas [1988, 1994], Jensen *et al.* [1989], Thomas [1996], and Klostermeyer [1998, 2001]. Satellite observations provided the first evidence of the water ice composition of PMC/NLC particles and the enhanced water vapor layer in the PMC/NLC region [Hervig *et al.*, 2001; Summers *et al.*, 2001; Stevens *et al.*, 2001].

[3] Since the first observation of noctilucent clouds by *Backhouse* [1885], PMC/NLC have been studied from ground by numerous visual, photographic, spectroscopic, photometric and polarimetric observations for more than a century as reviewed by *Gadsden and Schröder* [1989]. PMC/NLC have also been investigated by in situ rocket experiments [e.g., *Witt*, 1969; *Gumbel and Witt*, 1998] and by space observations from the satellites OGO-6, SME, NIMBUS 7, UARS, SPOT 3, MSX and METEOSAT 5 [e.g., *Donahue et al.*, 1972; *Thomas and Olivero*, 1989; *Thomas et al.*, 1991; *Evans et al.*, 1995; *Debrechtian et al.*, 1997; *Carbary et al.*, 1999; *Gadsden*, 2000] in both hemispheres. Numerous lidar observations in the northern hemisphere provide precise information on PMC/NLC altitude, layer vertical structure and backscatter coefficient and valuable information on particle size, diurnal variation and wave signatures [e.g., *Hansen et al.*, 1989; *Thomas et al.*, 1994; *Thayer et al.*, 1995; *von Cossart et al.*, 1996; *von Zahn et al.*, 1998; *Alpers et al.*, 2000; *Gardner et al.*, 2001; *Thayer et al.*, 2002].

[4] The first lidar observations of PMC at the South Pole and in the southern hemisphere were made by *Chu et al.* [2001a, 2001b] with an Fe Boltzmann temperature lidar in the 1999–2000 austral summer season at the Amundsen-Scott South Pole Station. A significant hemispheric difference in PMC altitudes was found from the first season data that the mean altitude of PMC at the South Pole is about 2–4 km higher than PMC/NLC in the northern hemisphere [*Chu et al.*, 2001a] including the PMC we observed over the geographic North Pole using the same lidar instrument 6 months earlier [*Gardner et al.*, 2001]. The lidar observations were continued and more extensive PMC data were obtained in the 2000–2001 austral summer season at the South Pole. Besides the hemispheric difference in PMC altitude and the interannual difference between two PMC seasons, the lidar data in both seasons exhibit clear seasonal trends of PMC altitude and backscatter coefficient, and clear diurnal and semidiurnal variations of PMC altitude and backscatter coefficient at the South Pole. In this paper, the interannual, seasonal and diurnal variations of PMC at the South Pole are studied in detail by using more than 430 h of PMC data obtained in these two seasons. The causes of the hemispheric difference in PMC altitude are also investigated by comparing lidar data with the predictions from the NCAR Thermosphere-Ionosphere-Mesosphere-Electrodynamics General Circulation Model (TIME-GCM) [*Roble and Ridley*, 1994; *Roble*, 2000]. The hemispheric difference in PMC altitude is attributed to the hemispheric differences in the altitudes of the supersaturation region and in the upwelling vertical wind, which are mainly caused by the different solar heating in the summer of the two hemispheres because of the orbital eccentricity of the Earth. Possible relation between mesospheric water vapor and PMC brightness are also discussed.

## 2. Lidar Data Processing

[5] The PMC observations were made by the University of Illinois Fe Boltzmann temperature lidar at 374 nm and 372 nm. The information about the lidar system and its measurement capabilities are described in considerable

detail by *Chu et al.* [2002]. The lidar photon count profiles were collected with a vertical resolution of 48 m, and then were smoothed by using a Hamming window with FWHM of 250 m. After subtracting the background photon counts and compensating for the range dependence of the signal levels, the profiles were integrated for one hour and normalized to the Rayleigh signal at 50 km to produce a normalized photon count profile. The PMC backscatter ratio  $R(z)$ , volume backscatter coefficient  $\beta(z)$ , total backscatter coefficient  $\beta_{\text{Total}}$ , centroid altitude  $Z_C$  and RMS width  $\sigma_{rms}$  are then derived from the hourly mean profile using the definitions and equations listed in Table A1 in Appendix A. The atmosphere number density, pressure and temperature used in the computation are taken from MSIS90 model (Mass Spectrometer Incoherent Scatter Extended Model). Since the backscatter ratio is not only dependent on PMC backscatter intensity but is also related to the atmosphere density at PMC height, it is more accurate to use volume backscatter coefficient  $\beta$  (instead of backscatter ratio  $R$ ) to present the PMC layer structure. Therefore, the centroid altitude and RMS width were computed from the volume backscatter coefficient profiles as illustrated in Table A1.

[6] Normally the system is operated with the lasers tuned to the two Fe resonance lines. The 372 nm line is the primary resonance line which is based on the lowest ground state ( $J = 4$ ) while the 374 nm line is based on an upper subground state ( $J = 3$ ) which is about  $416 \text{ cm}^{-1}$  above the lowest state [*Chu et al.*, 2002]. The populations on these two states obey the Maxwell-Boltzmann distribution in thermal equilibrium. For typical midlatitude mesopause region temperatures ( $\sim 200 \text{ K}$ ) the backscatter signal from the 374 nm line is about 30 times weaker than that from the 372 nm line. Although a small amount of backscatter from the 372 nm Fe line may exist in the range of 82–86 km where PMC are typically observed, the backscatter from the 374 nm line is very small because the population on  $J = 3$  subground state under typical summer mesospheric temperature above the South Pole ( $< 150 \text{ K}$ ) is about 80 times lower than the population on  $J = 4$ . Consequently, the backscatter from the 374 nm Fe line is typically less than 1% of PMC backscatter. The backscatter coefficients derived from 374 nm data can be regarded as the actual values of PMC. During routine observations both lasers were periodically detuned 10 GHz off the Fe resonance lines to confirm the existence of PMC. When PMC signals appear, both 374 nm and 372 nm channels should show the similar signal at the same height. This is also one of our criteria for distinguishing PMC signals from background noise.

## 3. Observations

[7] We initially deployed the Fe Boltzmann temperature lidar aboard the NSF/NCAR Electra aircraft and flew to the North Pole in June and July of 1999 to study the temperature structure of the summer Arctic mesopause region. During this campaign, PMC were observed over the North Pole ( $90^\circ\text{N}$ ) and Gulf of Alaska ( $58^\circ\text{N}$ ) [*Gardner et al.*, 2001]. The Fe lidar was then installed at Amundsen-Scott South Pole Station in late November of 1999 to characterize the atmospheric temperature structure, PMC and Fe layers

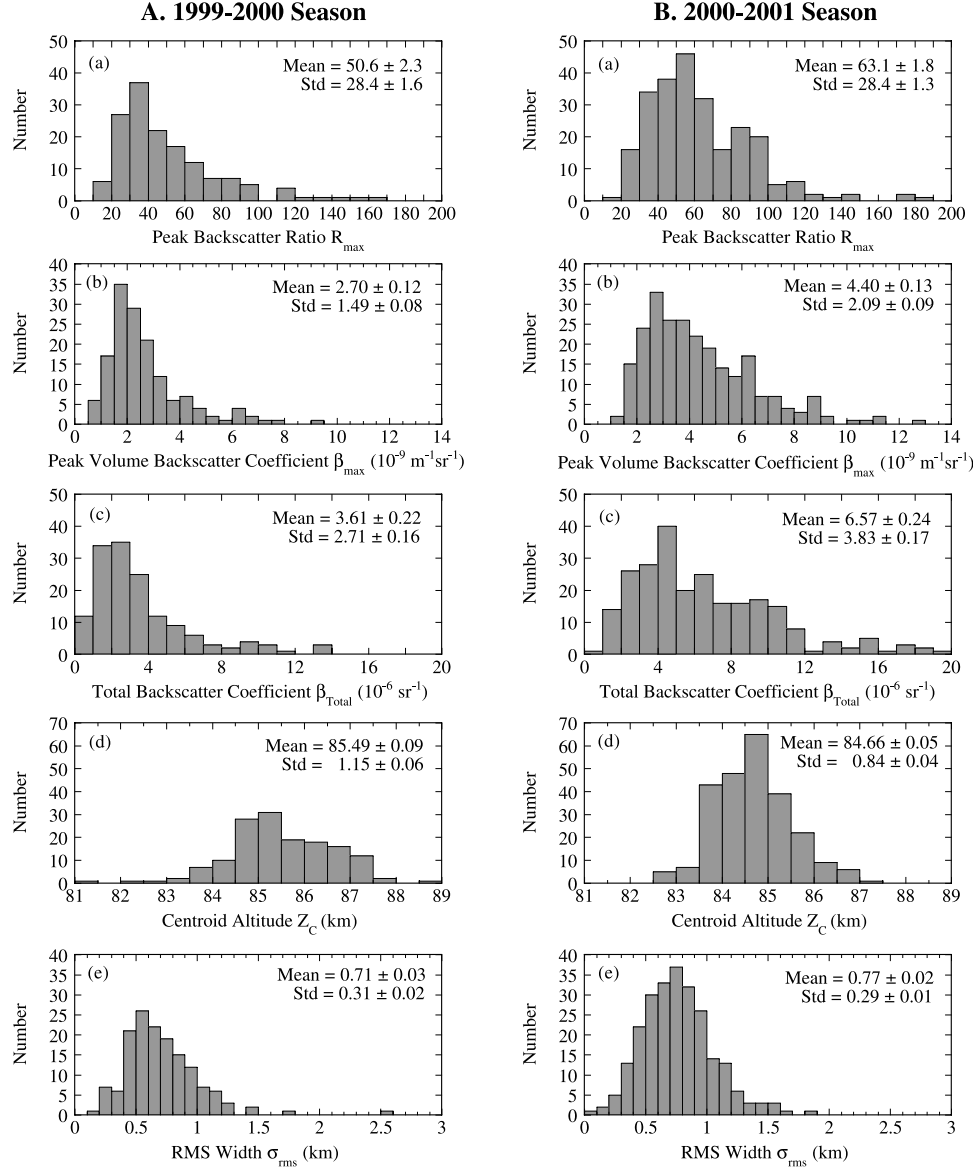


**Figure 1.** Histograms of PMC characteristics in the 1999–2000 and 2000–2001 summer seasons at the South Pole.

[Chu et al., 2001a, 2001b; Gardner et al., 2001]. Extensive PMC data sets were collected at South Pole in 1999–2000 and 2000–2001 summer seasons.

### 3.1. Interannual Variations in PMC

[8] During the 1999–2000 summer season, PMC were observed beginning on 11 December 1999 and ending on 24 February 2000. During this 76 day period, PMC were observed for a total of 192 h and the occurrence probability was 66.5% [Chu et al., 2001a]. During the 2000–2001 summer season, PMC were observed beginning on 24 November 2000 and ending on 6 February 2001. During this 75 day period, PMC were observed for a total of 245 h and the occurrence probability was 67.9%.

[9] Histograms of the measured hourly mean PMC peak backscatter ratio  $R_{\max}$ , peak volume backscatter coefficient  $\beta_{\max}$ , total backscatter coefficient  $\beta_{\text{Total}}$ , layer centroid altitude  $Z_C$  and layer RMS width  $\sigma_{\text{rms}}$  are plotted in Figure 1 for

1999–2000 and 2000–2001 seasons. The standard deviation of each parameter distribution is also illustrated in Figure 1. The mean characteristics of the PMC and their uncertainties observed during these two seasons are summarized in Table 1. The most significant differences between the two seasons are in PMC brightness (backscatter coefficients) and altitudes. The mean total backscatter coefficient of PMC in the 2000–2001 season is 82% larger than in the 1999–2000 season, while the mean centroid altitude of PMC in the 2000–2001 season is 0.83 km lower than in the 1999–2000 season.

[10] The total backscatter coefficient of PMC layers distributed from  $0.48 \times 10^{-6} \text{ sr}^{-1}$  to  $13.75 \times 10^{-6} \text{ sr}^{-1}$  in the 1999–2000 season and from  $0.81 \times 10^{-6} \text{ sr}^{-1}$  to  $19.66 \times 10^{-6} \text{ sr}^{-1}$  in the 2000–2001 season. The peak volume backscatter coefficients ranged from  $0.75 \times 10^{-9} \text{ m}^{-1} \text{ sr}^{-1}$  to  $9.35 \times 10^{-9} \text{ m}^{-1} \text{ sr}^{-1}$  and from  $1.29 \times 10^{-9} \text{ m}^{-1} \text{ sr}^{-1}$  to  $12.93 \times 10^{-9} \text{ m}^{-1} \text{ sr}^{-1}$  in the 1999–2000 and 2000–

**Table 1.** Mean Characteristics of the PMC Observed at the South Pole During the 1999–2000 and 2000–2001 Summer Seasons

	1999–2000 Season	2000–2001 Season	Overall Mean
Peak backscatter ratio $R_{\max}$	$50.6 \pm 2.3$	$63.1 \pm 1.8$	$58.4 \pm 1.5$
Peak volume backscatter coefficient $\beta_{\max} \times 10^{-9} \text{ m}^{-1} \text{ sr}^{-1}$	$2.70 \pm 0.12$	$4.40 \pm 0.13$	$3.75 \pm 0.10$
Total backscatter coefficient $\beta_{\text{Total}} \times 10^{-6} \text{ sr}^{-1}$	$3.61 \pm 0.22$	$6.57 \pm 0.24$	$5.45 \pm 0.19$
Centroid altitude $Z_C$ , km	$85.49 \pm 0.09$	$84.66 \pm 0.05$	$85.03 \pm 0.05$
Layer RMS width $\sigma_{rms}$ , km	$0.71 \pm 0.03$	$0.77 \pm 0.02$	$0.75 \pm 0.02$
Occurrence probability	66.5%	67.9%	67.4%
PMC period	11 December 1999 to 24 February 2000 (76 days)	24 November 2000 to 6 February 2001 (75 days)	

2001 seasons, respectively. Most of the PMC belong to the strongest classes according to the computed classification for NLC displays listed in the work of Meriwether *et al.* [1993], and they are much brighter than the NLC observed at Sondrestrom, Greenland [Thayer *et al.*, 2002]. The range of peak backscatter ratio at the South Pole was from 10.0 to 162.2 in the 1999–2000 season and from 17.7 to 185.2 in the 2000–2001 season.

[11] The PMC layer RMS width ranged from 0.19 km to 2.54 km in the first season and from 0.10 km to 1.85 km in the second season. Their mean values are similar. The PMC centroid altitude ranges from 81.06 to 88.55 km in the first season, and from 82.57 to 87.14 km in the second season. The mean PMC altitudes of  $85.49 \pm 0.09$  km and  $84.66 \pm 0.05$  km in two seasons are 2–3 km higher than PMC/NLC observed elsewhere. They are also higher than the PMC altitude  $83.2 \pm 1.4$  km measured by satellite near the South Pole [Carbary *et al.*, 2001a].

### 3.2. Seasonal Variations in PMC

[12] The seasonal variations of the hourly mean PMC peak backscatter ratio  $R_{\max}$ , peak volume backscatter coefficient  $\beta_{\max}$ , total backscatter coefficient  $\beta_{\text{Total}}$ , centroid altitude  $Z_C$  and layer RMS width  $\sigma_{rms}$  are plotted versus day number relative to summer solstice in Figure 2 for both 1999–2000 and 2000–2001 seasons. Figure 2 shows that the PMC season can start as early as about 30 days before summer solstice, and can end as late as about 70 days after summer solstice. The occurrence probability was computed for each two-week period during the PMC season and the results are plotted versus day number in Figure 3. The highest occurrence probability, almost 90%, occurs between 25 and 40 days after solstice during both seasons.

[13] The backscatter ratio and coefficients exhibit considerable scatter with both parameters varying over a range of more than an order of magnitude during both seasons. This is associated with the strong diurnal variations of PMC [Chu *et al.*, 2001b]. To investigate the possible trend behind the scattered data, we smoothed the total backscatter coefficient using triangular smooth for each data point. The smoothing full width is 11 days. The result is illustrated in Figure 4a. It clearly shows that the 2000–2001 season PMC is much brighter than the 1999–2000 season, and both seasons exhibit maximum brightness in the period of 25–40 days after summer solstice, which is also the period when occurrence probabilities reach maximum in both seasons. The trend of PMC brightness is approximately consistent with the trend of PMC occurrence probability as shown in Figure 3. This agrees with the satellite finding that PMC are

brightest right where and when they occur most frequently [Thomas and Olivero, 1989].

[14] Significant seasonal trends emerge from the scattered PMC altitude data as shown in Figures 2g and 2h. To better illustrate these trends, a 11-day triangle smooth was applied to PMC altitudes and smoothed PMC altitudes are plotted in Figure 4b. During both seasons, since 10 days before summer solstice, the altitudes generally increase as the season progresses, reaching maximum values around 10–20 days after summer solstice, and then decrease throughout the remainder of the season. PMC altitudes exhibit similar descending rate from about 18 to 50 days after solstice in both seasons. As pointed out by Chu *et al.* [2001a] based on the 1999–2000 season data, PMC altitudes decrease by about 64 m/day from day 18 to day 53 after solstice. A linear fit to the 2000–2001 season data from day 18 to day 48 gives a decreasing rate of 65 m/day. However, at the beginning of 2000–2001 season, PMC altitudes start at a relatively high value of 85 km, and then decrease to slightly below 84 km around 10 days before solstice. Due to lack of data in that period, this feature does not appear in the 1999–2000 season data.

[15] There is no obvious seasonal trend occurring in the PMC layer RMS width as shown in Figures 2i and 2j. The RMS width is approximately homogeneous throughout most of the PMC seasons. This is confirmed by the 11-day triangle smoothed data shown in Figure 4c.

### 3.3. Diurnal Variations in PMC

[16] Significant diurnal variations have been observed in PMC backscatter coefficients and altitudes, which were attributed to tidal variations in temperature and vertical wind caused by a zonally symmetric tide at the South Pole [Chu *et al.*, 2001b] and a stable semidiurnal tide at Andoya ( $69^{\circ}\text{N}$ ) [von Zahn *et al.*, 1998]. A clear in-phase relationship between backscatter coefficients and altitudes was found at the South Pole in the first season [Chu *et al.*, 2001b]. In contrast, a clear out-of-phase relationship was observed at Andoya [von Zahn *et al.*, 1998]. More data obtained in the second season at the South Pole allows us to further investigate the diurnal variations. Histograms of the total observation hours and occurrence probabilities for both seasons are plotted versus UT hour in Figure 5. (Here, the occurrence probability for each UT hour is the ratio of the hours PMC appeared to the total observation hours in each UT hour during PMC season.) The total observation time in each UT hour varied over a factor of four in the 1999–2000 season with as low as 4 h of data between 2300 and 0200 UT and as high as 16 h of observations between 1000 and

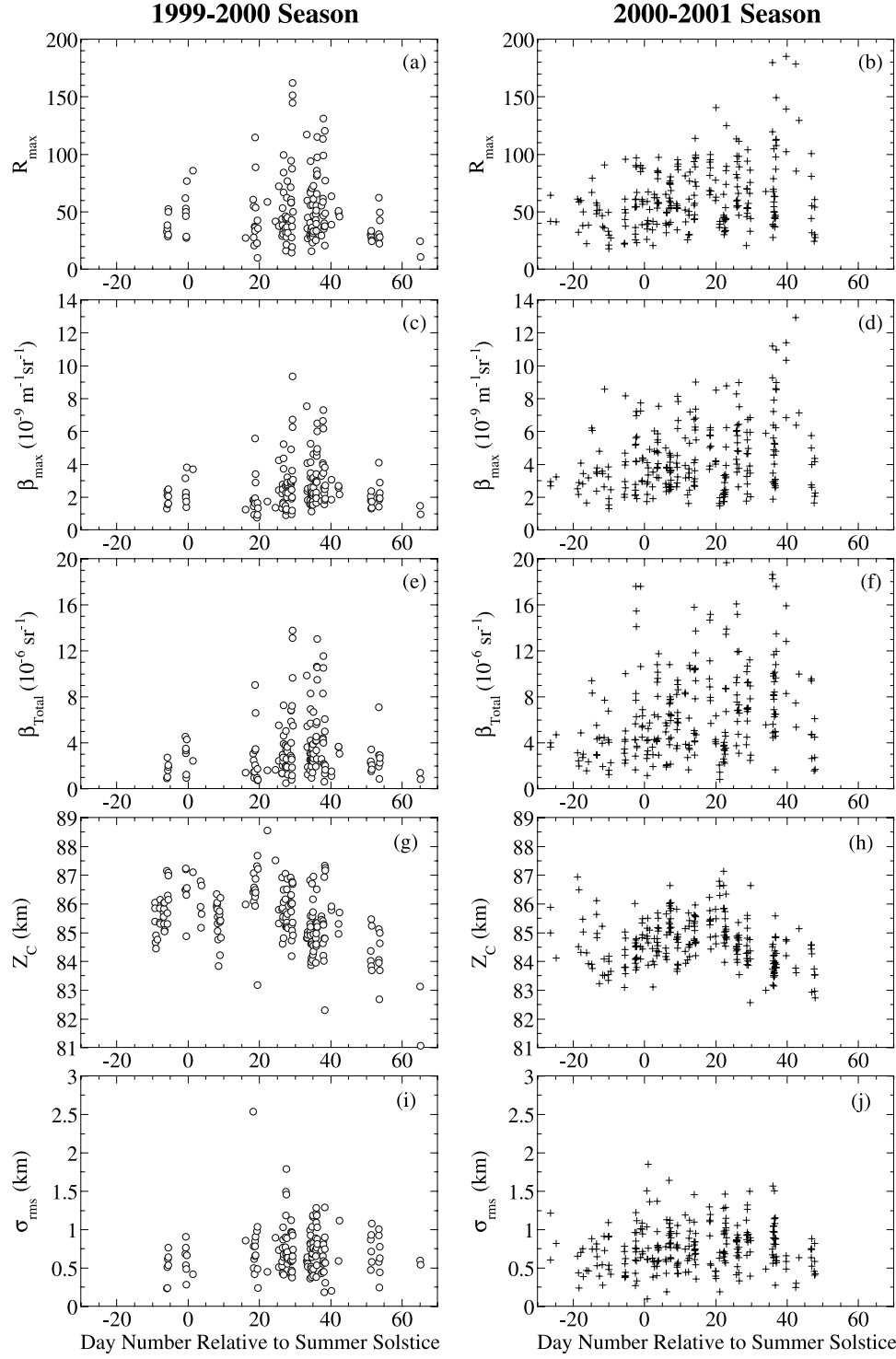


**Figure 2.** Seasonal variations of hourly mean PMC parameters versus day number relative to summer solstice (21 December) in the 1999–2000 (o) and 2000–2001 (+) summer seasons at the South Pole: (a, b) peak backscatter ratio; (c, d) peak volume backscatter coefficient; (e, f) total backscatter coefficient; (g, h) centroid altitude; (i, j) layer RMS width.

1100 UT. PMC occurrence probability was surprisingly constant at about 70% throughout the day except between 1300 and 1400 UT when the occurrence probability fell to only 10%. The distribution of observation time was more uniform when more data were collected during the 2000–

2001 season. Like the first season the PMC occurrence probability was relatively constant at about 70% throughout the day except between 1300 and 1400 UT when it fell to 37%. The drop in occurrence probability between 1300 and 1400 UT in both seasons indicates poor forming conditions

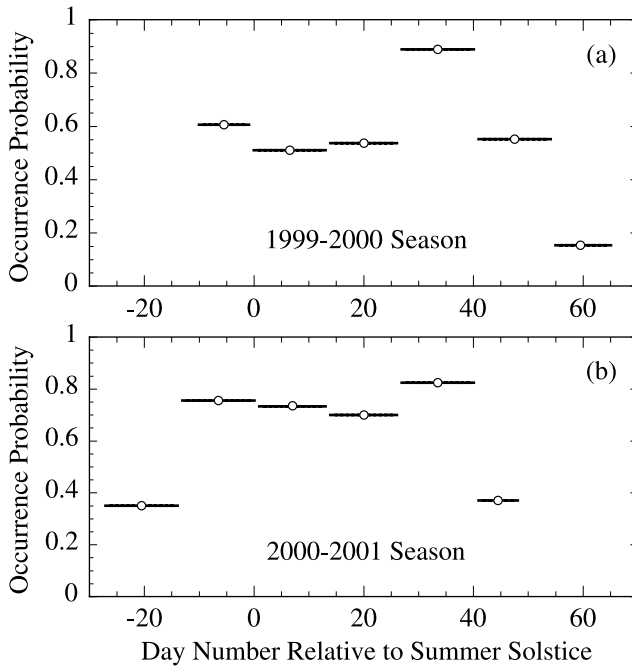


**Figure 3.** PMC occurrence probability versus day number relative to summer solstice in (a) 1999–2000 and (b) 2000–2001 summer seasons at the South Pole.

for PMC during this period at the South Pole. We think it may be related to the effects of the zonally symmetric semidiurnal tide [Chu et al., 2001b]. Modeling efforts are needed to fully understand this feature.

[17] The mean total backscatter coefficient and centroid altitude of PMC for each hour of the day are plotted versus UT hour in Figures 6a and 6b. The solid curves are the diurnal plus semidiurnal harmonic fits to the data as shown in equation (1):

$$y = A_0 + A_{12} \cos\left[\frac{2\pi}{12}(t - UT_{12})\right] + A_{24} \cos\left[\frac{2\pi}{24}(t - UT_{24})\right]. \quad (1)$$

The fitting parameters are summarized in Table 2. Although the diurnal variations of  $R_{\max}$  and  $\beta_{\max}$  are not plotted here, their fitting parameters are also summarized in Table 2 for comparison. Notice that both the backscatter coefficient and altitude exhibit two peaks around 0630 and 1930 UT, and both exhibit a minimum between 1300 and 1400 UT. But while the peak for backscatter coefficients around 0630 UT is significantly smaller than the peak around 1930 UT, the PMC altitude has much larger peak around 0630 UT than around 1930 UT. There is an in-phase relation for the 12-h oscillation and an out-of-phase relation for the 24-h oscillation between PMC backscatter coefficient and centroid altitude. The fitting parameters in Table 2 show that the backscatter coefficient and the altitude have similar phase around 0730 UT in semidiurnal variation (12-h), while their phases in diurnal variation (24-h) are almost opposite to each other. The phase difference is about 16 h in diurnal variation. Meanwhile, the backscatter coefficient has similar amplitudes in semidiurnal and diurnal variations, but

the altitude has a larger amplitude in diurnal variation than in semidiurnal variation. The observed diurnal oscillations in Figure 6 may be explained as the following: the positive-correlation between backscatter coefficient and the altitude is caused by the in-phase semidiurnal variation, while the anti-correlation between the maxima of backscatter coefficient and altitude is determined by the out-of-phase diurnal variation.

[18] In Chu et al. [2001b], the semidiurnal variation dominated the altitude while the backscatter coefficient had similar amplitudes in semidiurnal and diurnal variations. The in-phase occurred in both semidiurnal and diurnal

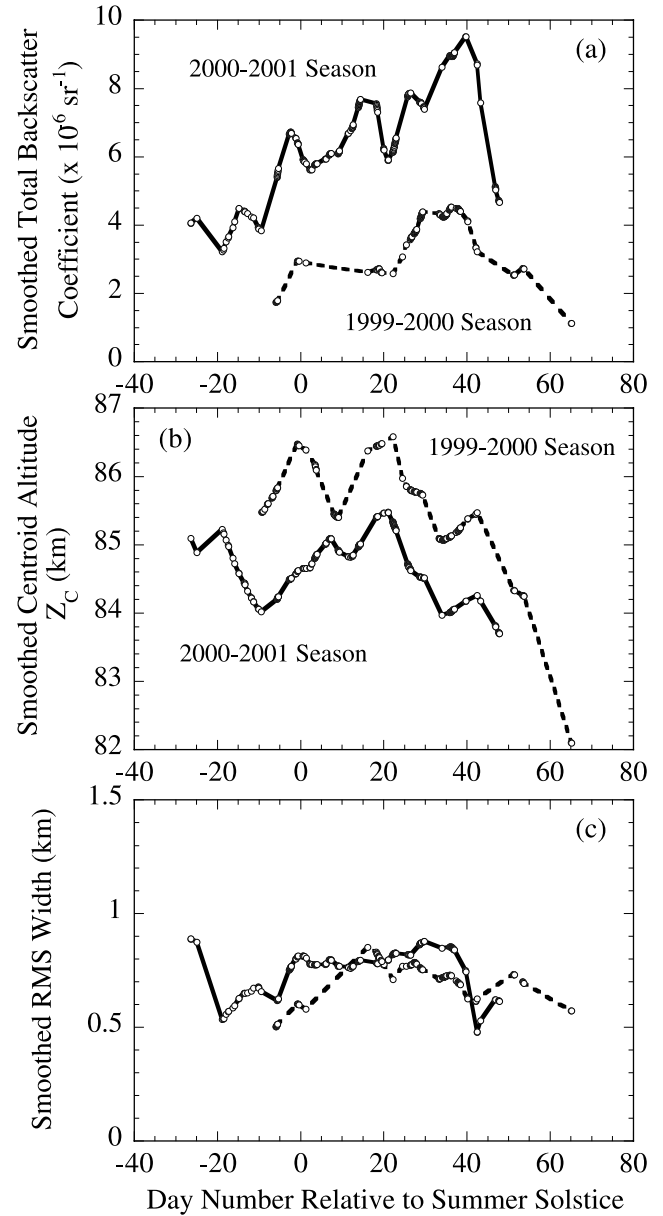


**Figure 4.** Eleven-day smoothed PMC parameters versus day number at the South Pole: (a) smoothed total backscatter coefficient; (b) smoothed centroid altitude; (c) smoothed RMS width. Circles are the smoothed data points, dashed line is for 1999–2000 season and solid line is for 2000–2001 season.

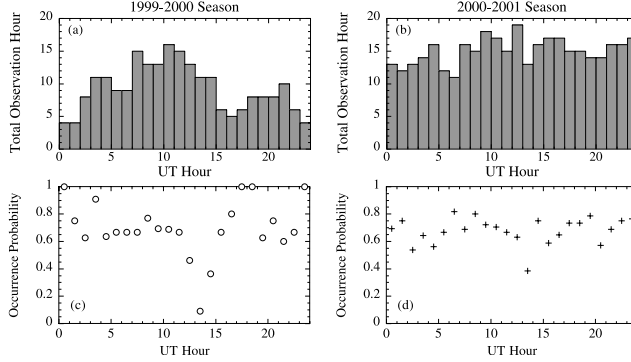


**Figure 5.** Total observation hours and PMC occurrence probability versus UT hour in 1999–2000 (o) and 2000–2001 (+) summer seasons at the South Pole.

variations [Chu et al., 2001b]. An example of out-of-phase correlation was observed in the 2000–2001 season on 26 January 2001 as shown in Figure 7. A harmonic fit containing of 24-h, 12-h and 8-h oscillations was applied to the total backscatter coefficient and centroid altitude. The fitting parameters are listed in Table 3. The phases of backscatter coefficient and altitude are almost opposite for all three variations. The amplitudes of three oscillations in backscatter coefficient are similar while the 24-h and 8-h oscillation amplitude in altitude are much larger than its 12-h amplitude.

[19] The PMC total backscatter coefficients are plotted versus PMC centroid altitude in Figure 8. The circles are for 1999–2000 season, and the crosses are for 2000–2001 season. The plot is quite different from those observed at Andoya and Sondrestrom [Thayer et al., 2002]. In the northern hemisphere, the largest backscatter coefficients are observed at the lowest altitudes, which is consistent with the current theory of PMC particles forming at higher altitudes near the mesopause and then falling to lower altitudes as they grow in size and mass. At the South Pole, the distribution is roughly symmetric and PMC exhibit the largest backscatter coefficients near the center of the altitude distribution around 85 km. The backscatter coefficients tend to be smaller both above and below the mean altitude.

#### 4. TIME-GCM Simulations of Atmosphere

[20] The NCAR Thermosphere-Ionosphere-Mesosphere-Electrodynamics General Circulation Model (TIME-GCM), after being tuned for equinox and solstice conditions, was run for an entire year. The solar activity level for the simulation was held constant at a representative of F10.7 value of 150, and the auroral parameters were held constant at quiet geomagnetic conditions. The lower boundary forcing of geopotential height and temperature were specified by an empirical model and gravity wave forcings were identical between hemispheres. The details of the year simulation were given by Roble [2000]. The year simulation included an orbital eccentricity variation of 6% with maximum solar heating occurring in January and minimum in July for present-day conditions. The model recorded histories daily at 00 UT and a diurnal cycle was recorded every 10 days throughout the year. The daily histories of the atmos-

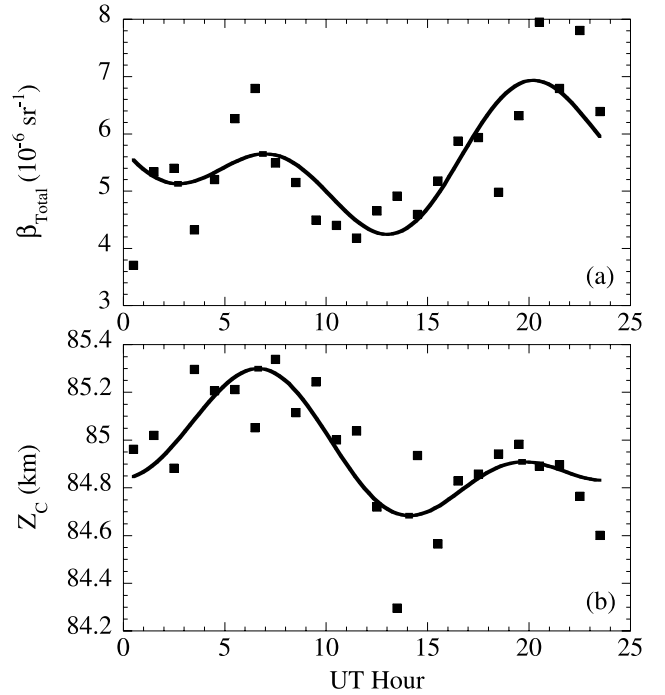


**Figure 6.** The mean PMC parameters averaged over two seasons versus UT hour at the South Pole: (a) mean total backscatter coefficient; (b) mean centroid altitude. The solid curves are the diurnal plus semidiurnal harmonic fits using equation (1).

pheric data from the TIME-GCM simulations are used in the following analysis. A detail description of the TIME-GCM simulations can be found in Appendix B.

#### 5. Study of Hemispheric Difference in PMC Altitudes

[21] A significant hemispheric difference in PMC altitudes was found through our lidar observations over both poles. The mean altitude of 437 h PMC in two seasons is 85.03 km, which is 2–3 km higher than the common PMC altitude (82–83 km) observed in the northern hemisphere. For example, the mean altitude of PMC/NLC measured by lidars are 83.26 km at the North Pole ( $90^{\circ}\text{N}$ ) [Gardner et al., 2001]; 82.6 km [Hansen et al., 1989], 83.0 km [von Cossart et al., 1997], 82.7 km [von Zahn et al., 1998], 82.5 km [von Cossart et al., 1999] at Andoya, Norway ( $69^{\circ}\text{N}$ ,  $16^{\circ}\text{E}$ ); 82.5 km at Sondrestrom, Greenland ( $67^{\circ}\text{N}$ ,  $51^{\circ}\text{W}$ ) [Thayer et al., 2002]; 81.8 km at Alaska Gulf ( $58^{\circ}\text{N}$ )

**Table 2.** Parameters for Diurnal and Semidiurnal Harmonic Fits to the Mean of PMC Data in Both Seasons

	$R_{\text{max}}$	$\beta_{\text{max}},$ $\times 10^{-9} \text{ m}^{-1} \text{ sr}^{-1}$	$\beta_{\text{Total}},$ $\times 10^{-6} \text{ sr}^{-1}$	$Z_C,$ km
$A_0$	$58.24 \pm 0.91$	$3.76 \pm 0.07$	$5.51 \pm 0.17$	$84.944 \pm 0.034$
$A_{12}$	$8.13 \pm 1.28$	$0.38 \pm 0.10$	$0.75 \pm 0.25$	$0.154 \pm 0.049$
$A_{24}$	$5.43 \pm 1.28$	$0.34 \pm 0.10$	$0.79 \pm 0.25$	$0.212 \pm 0.049$
$UT_{12}$	$7.42 \pm 0.30$	$7.59 \pm 0.53$	$7.74 \pm 0.63$	$7.02 \pm 0.60$
$UT_{24}$	$23.20 \pm 0.90$	$21.29 \pm 1.16$	$22.06 \pm 1.19$	$5.57 \pm 0.87$
Correlation Coefficient	86.9%	74.8%	71.2%	77.9%

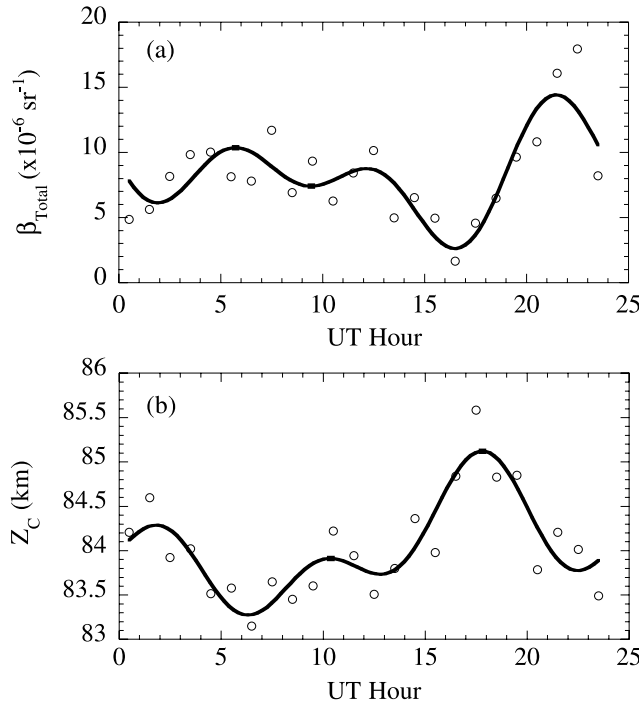


**Figure 7.** Diurnal variations of PMC parameters versus UT hour on 26 January 2001 at the South Pole: (a) total backscatter coefficient; (b) centroid altitude. The solid curves are the harmonic fits of 24-h, 12-h and 8-h.

[Gardner *et al.*, 2001]; 83.4 km at Juliusruh ( $54.63^{\circ}\text{N}$ ,  $13.38^{\circ}\text{E}$ ) [von Cossart *et al.*, 1996].

[22] The formation and evolution of PMC particles is a complex process that depends on the temperature, water vapor and vertical wind structures of the mesopause region. PMC particles actually consist of water ice, and the water ice particles are only formed in the supersaturation region where water vapor pressure  $P_w$  is higher than saturation water vapor pressure  $P_s$ , or in other words, the atmosphere temperature  $T$  is lower than the frost point  $T_s$ . Once they fall into the subsaturation region where  $P_w < P_s$ , the ice particles will be destroyed quickly by sublimation due to higher temperatures at lower altitudes [Thomas, 1991]. Therefore, PMC altitudes will be determined primarily by the altitude of supersaturation region. To study the possible causes for this hemispheric difference in PMC altitudes, we use data from the TIME-GCM to represent the temperature, water vapor and vertical wind structures of atmosphere at the poles. The supersaturation regions at the South Pole and the North Pole predicted by TIME-GCM are plotted in Figure 9 along with two seasons PMC data at the South Pole. The lines denote the boundary where the atmosphere temperature is equal to the frost point. The scattered points on Figure 9 are our lidar data of PMC at the South Pole. They mainly stay within the saturation region clustered along its bottom. Comparing the saturation regions at the South and North Poles, we find that the South Pole saturation region is generally 2–3 km higher than the North Pole saturation region. This hemispheric difference in supersaturation region altitudes is approximately equal to the hemispheric difference in PMC altitudes found by our lidar measurements over both poles.

**Table 3.** Parameters for Harmonic Fits to the PMC Data on 26 January 2001 at the South Pole

	$\beta_{\text{Total}} \times 10^{-6} \text{ sr}^{-1}$	$Z_C$ , km
$A_0$	$8.29 \pm 0.48$	$84.046 \pm 0.066$
$A_{24}$	$1.82 \pm 0.67$	$0.534 \pm 0.093$
$A_{12}$	$2.62 \pm 0.67$	$0.204 \pm 0.093$
$A_8$	$2.58 \pm 0.67$	$0.389 \pm 0.093$
$UT_{24}$	$1.28 \pm 1.41$	$18.63 \pm 0.67$
$UT_{12}$	$9.47 \pm 0.49$	$4.65 \pm 0.88$
$UT_8$	$5.19 \pm 0.33$	$1.92 \pm 0.31$
Correlation Coefficient	82.8%	87.4%

[23] Once PMC particles form in the saturation region around mesopause, under gravitational pull, the PMC particles will slowly settle down through the supersaturation region while growing in size and mass. The particles also experience a buoyancy force mainly due to the upwelling atmosphere over the summer pole. When the buoyancy force of the upwelling atmosphere balances the gravitational force on the PMC particle, PMC particles will stay around that altitude, which is a few km below mesopause, and PMC layers will be observed there. (See Appendix C for a detail discussion. Briefly, the terminal fallspeed of cloud particles in the rest atmosphere is reached when the net upward force exactly balances the downward gravitational force on the falling particle [Reid, 1975]. The net upward force is due to the difference in velocity between the atmosphere molecules striking the particle from below or those from above caused by the particle falling speed. When there is no upwelling vertical wind, i.e., in the rest atmosphere, the terminal fallspeed is usually nonzero, so the cloud particles will continue falling down. When the upwelling vertical wind presents, the particle fallspeed can be compensated by the upwelling vertical wind and the terminal fallspeed of cloud particles in the rest frame of the Earth ground can be zero.)

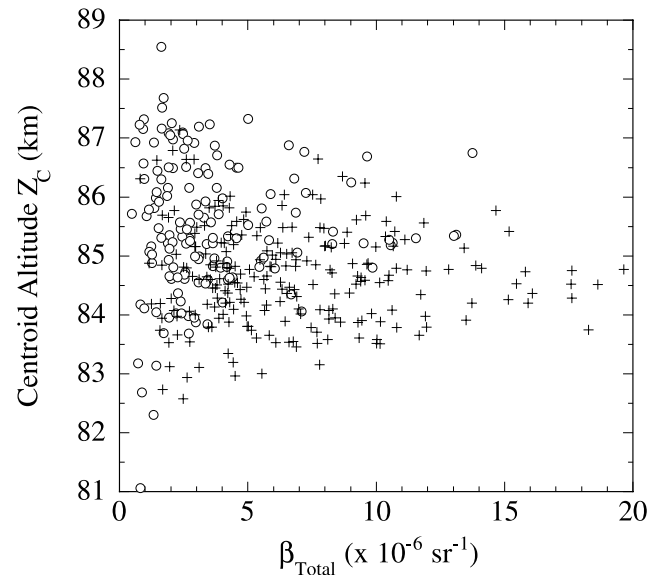


**Figure 8.** PMC total backscatter coefficients versus centroid altitudes for the 1999–2000 (o) and 2000–2001 (+) summer seasons at the South Pole.

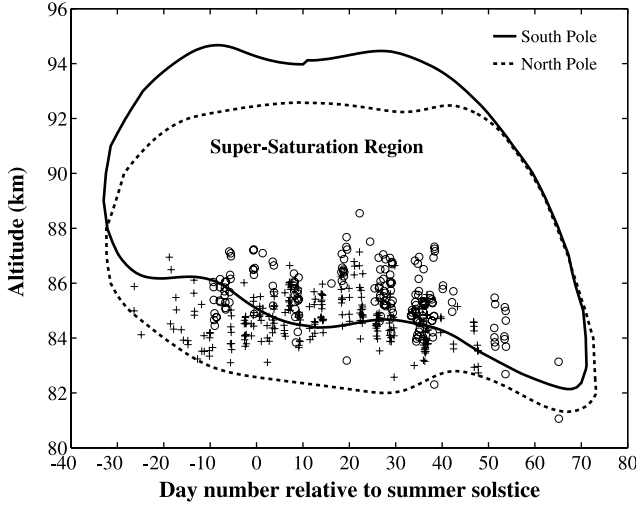


**Figure 9.** Supersaturation regions predicted by the TIME-GCM at the South and North Poles. The lines denote the boundary where the atmosphere temperature is equal to the frost point. Scattered data points are South Pole PMC data in (o) 1999–2000 season and (+) 2000–2001 season.

Therefore, within the saturation region, the PMC altitude will be confined by the following force balance equation:

$$mg = C\rho(z, d, \theta)w(z, d, \theta) \quad (2)$$

where  $m$  is the mass of individual PMC particle,  $g$  is gravitational acceleration,  $C$  is the drag coefficient,  $\rho(z, d, \theta)$  is the atmosphere density at altitude  $z$  on day number  $d$  at latitude  $\theta$ ,  $w(z, d, \theta)$  is the atmosphere vertical wind for similar conditions.

[24] Because atmospheric density is smaller at higher altitude and this buoyancy provided by the upwelling air is proportional to the product of atmospheric density and vertical wind, a higher vertical wind is required to maintain the South Pole PMC staying at 2–3 km higher altitudes than the North Pole if PMC particle mass and drag coefficient are similar at both Poles. Plotted in Figure 10 is an example of the vertical profile of temperature and vertical wind at the South and North Poles on the 13th day after summer solstice predicted by TIME-GCM. The vertical wind is about 3.5 cm/s around 85 km at the South Pole, which is larger than the vertical wind of 2.5 cm/s around 83 km at the North Pole. The South Pole mesopause ( $\sim 91$  km) is about 2 km higher than the North Pole mesopause ( $\sim 89$  km), just as the South Pole saturation region is about 2–3 km higher than North Pole shown in Figure 9. Meanwhile, the South Pole mesopause is about 7 K colder than the North Pole mesopause. The PMC layers are higher at the South Pole because they begin forming in the higher saturation region near the higher mesopause. As they grow in size and slowly fall to lower altitudes within the supersaturation region, the larger vertical wind of upwelling atmosphere at the South Pole would provide sufficient buoyancy to maintain the PMC particles at altitudes that are about 2–3 km higher than at the North Pole. Thus, the South Pole PMC are expected to be higher than the North Pole PMC as we observed. The features of temperature and vertical wind

predicted by TIME-GCM are generally consistent with our observational results.

[25] Checking with the simulation of TIME-GCM, the hemispheric differences in mesopause altitudes and upwelling wind are mainly caused by the solar flux in January being 6% greater than the solar flux in July because of the Earth's orbital eccentricity where the Earth is closest to the Sun on 3 January and farthest from the Sun on 5 July. The increased solar heating at the South Pole during austral summer results in a warmer stratopause that causes a dynamic adjustment. The dynamic adjustment results in higher mesopause altitude and stronger upwelling vertical winds in summer at the South Pole than at the North Pole. These differences cause the supersaturation region to be at higher altitudes over the South Pole than over the North Pole (see Appendix B for details). Besides the hemispheric

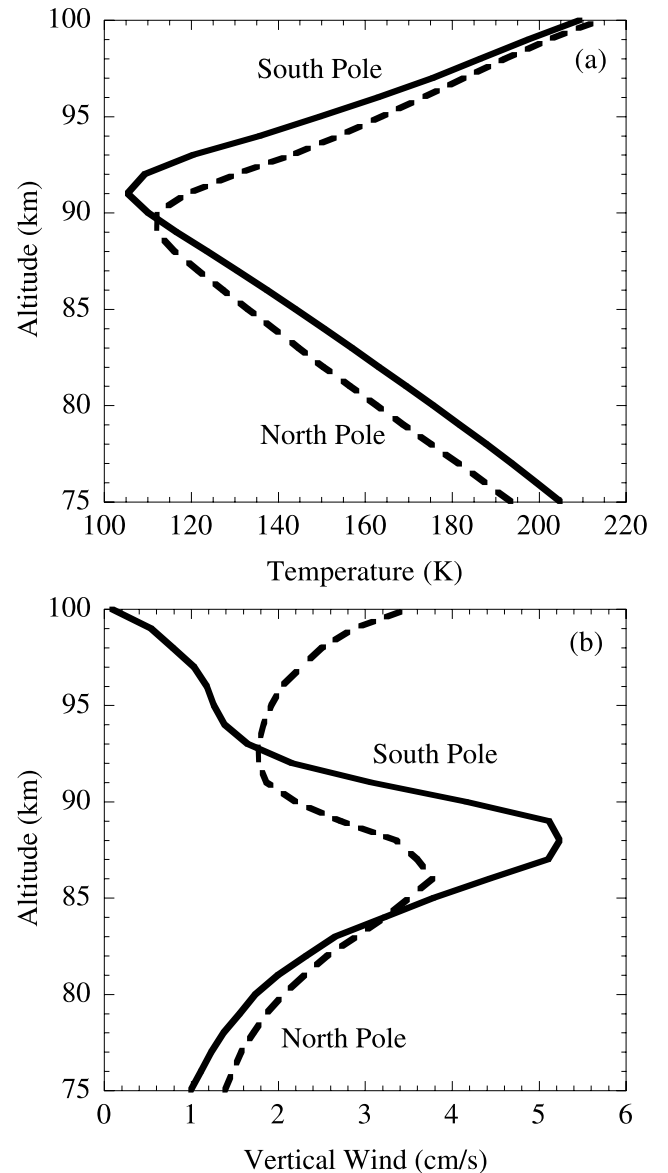


**Figure 10.** Vertical profiles of (a) temperature and (b) vertical wind on the 13th day after summer solstice at the South Pole (3 January, solid line) and the North Pole (4 July, dashed line) predicted by the yearlong run TIME-GCM.

differences in PMC altitudes, the lidar observations we made in similar seasons in two different years also indicate major interannual differences. In an attempt to understand possible differences, two identical TIME-GCM runs were made assuming perpetual December solstice conditions where the only difference between the two was the 6% variation of solar flux. All other model inputs remained constant and only the self-consistent physical and chemical processes internal to the model varied. The results showed that for the case with 6% more solar flux, the upper stratosphere and mesosphere warmed by about 4K and the mesopause moved upward about 1 km and cooled about several ( $\sim 5$  K) degrees. The change in structure altered the transmission of gravity waves and the altered momentum deposition and pressure gradients caused the westward winds to increase in the summer hemisphere and eastward winds to increase in the winter hemisphere. This dynamic adjustment resulted in an increase of vertical winds in the mesopause region. The 1 km increase in the mesopause caused by the solar flux variation is not as great as the 2–3 km hemispheric difference observed by the lidar. This indicates that the model solar forcing variations alone cannot account for all of the observed variation between hemispheres nor the interannual variability and that some variations in gravity wave forcing are involved in the mesopause location. Undoubtedly, the residual differences between hemispheres and the interannual differences at the south pole are dynamically forced probably related to gravity wave and planetary wave variability. Nevertheless, we believe that the main process responsible for the hemispheric differences is related to the difference in solar heating by the Earth's orbital eccentricity and that there is considerable dynamic variability superimposed the measurements. Detailed discussion about the above test can be found in Appendix B.

[26] We notice that on Figure 9, there are some PMC data points locating below the lower boundary of South Pole saturation region by 2–3 km, especially at the beginning of PMC seasons. This is probably because the TIME-GCM was not simulated for the specific years of PMC in 1999–2001. The model needs further tuning to match the PMC observational results. The present TIME-GCM simulations are qualitatively consistent with PMC data.

## 6. Discussions

[27] The supersaturation region and upwelling vertical wind predicted by TIME-GCM suggest that the PMC in the southern hemisphere should be higher than in the northern hemisphere, which has been confirmed by our lidar observations in both hemispheres. For satellite observations, *Thomas and Olivero* [1986] reported that the PMC height in northern hemisphere ( $85.0 \pm 1.5$  km) was about 2 km higher than in the south ( $83.2 \pm 1.5$  km) from 1981 to 1985. It is not clear what causes these contradictions between the SME satellite [*Thomas and Olivero*, 1986] and lidar observations. Satellites usually have limited vertical resolution whereas lidar provides much better vertical resolution in determining PMC altitude. *Carbary et al.* [2001a, 2001b] reported that the southern PMC were a little higher than their northern counterparts between 1997 and 1999 from MSX satellite measurements, although the south altitude

( $83.2 \pm 1.4$  km) and the north altitude ( $82.6 \pm 1.3$  km) are the same within statistical variations.

[28] We recognize some measurements made around 60–70 degrees latitude in both hemispheres that indicate that the southern hemisphere is warmer than the northern hemisphere, especially between 80 and 88 km [e.g., *Lübken et al.*, 1999; *Huaman and Balsley*, 1999; *Woodman et al.*, 1999; *Dowdy et al.*, 2001]. Since none of them are close to the pole region, these measurement may not properly reflect conditions right at the pole. However, as shown for the TIME-GCM data plotted in Figure 10a, the South Pole mesopause altitude is higher than the North Pole by about 2 km and colder by 5–10 K. Below the mesopause, between 80 and 88 km, the South Pole is warmer than the North Pole by 5–10 K, which is consistent with the measurements mentioned above. Thus, the TIME-GCM prediction of a higher and colder mesopause in summer at the South Pole is consistent with the region below the mesopause being warmer.

[29] PMC brightness is mainly determined by the PMC particle size and particle number density, which are related to the available water vapor amount and the time length that PMC particles can spend within the saturation region before they fall out. Using TIME-GCM predictions, we calculate the available water vapor pressure, which is the difference between actual water vapor pressure and saturation water vapor pressure. The saturation water vapor pressure is calculated from the neutral temperature data using the equation given by *Gadsden* [1981]:

$$\ln P_S(T) = 28.548 - \frac{6077.4}{T} \quad (3)$$

where  $P_S(T)$  is the saturation water vapor pressure at temperature T. We compute the vertical profiles of available water vapor density, and then integrate the available water vapor density within the saturation region for each day, and plot the results versus day number in Figure 11. Smoothed total backscatter coefficients of South Pole PMC data are also plotted on Figure 11. According to Figure 11, the available water vapor (i.e., saturation region) occurs between about 30 days before summer solstice and 70 days after summer solstice. This period agrees well with our lidar observations at the South Pole where the PMC were recorded during the period from 24 November to 24 February, which corresponds to –28 to 65 days around solstice. The lidar PMC data are within the available water vapor amount time period with an approximately similar shape. But the water vapor abundance does not explain the observed peak of backscatter coefficients around 25–40 days after solstice. It may involve a complicated microphysical process of how PMC particles form and develop. Satellite observations show that PMC occurrence frequency and brightness have strong dependence on day number and latitudes [*Thomas and Olivero*, 1989; *Carbary et al.*, 2001b]. The PMC period begins around 20–40 days before solstice and ends at about 60 days after solstice. The occurrence frequency and brightness both reach maximum about 3 weeks after solstice when the mesopause temperature is minimum [*Thomas and Olivero*, 1989]. We also integrate the available water density for each latitude in both hemispheres for 13 days after solstice. The results are

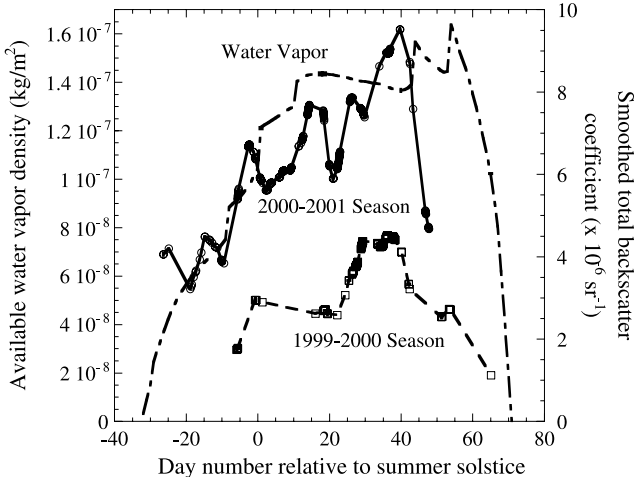


**Figure 11.** Integrated available water vapor density versus day number at the South Pole predicted by TIME-GCM shown as the dashed-dot line. Also plotted are 11-day smoothed total backscatter coefficient of PMC versus day number at the South Pole. Squares and dashed line are for 1999–2000 season, and circles and solid line are for 2000–2001 season.

plotted in Figure 12. The available water vapor density is strongly dependent on latitude, and more water vapor appears at higher latitudes. The latitudinal dependence of available water vapor content may explain the latitudinal dependence of PMC occurrence frequency observed by the satellites that higher PMC occurrence frequency occurs at higher latitudes [Thomas and Olivero, 1989].

[30] Figure 12 also shows that the northern hemisphere has more available water vapor than the southern hemisphere. There are a few possible factors that could contribute to the hemispheric difference in available water vapor content. The main factor would be that the altitude of northern saturation region is lower than the southern region. Since water vapor density increases exponentially with decreasing height, the northern saturation region at lower altitude would contain more water vapor than the southern saturation region at higher altitude. Besides, as pointed out by Garcia [1989], the solar Lyman- $\alpha$  flux at 121.6 nm can dissociate water vapor molecules, so the mesospheric water vapor is strongly affected by the solar flux. The more solar flux received in southern hemisphere summer caused by the Earth's orbital eccentricity would result in lesser water vapor in southern hemisphere. However, being opposite to the effect of greater photolysis rate in the south, the larger upwelling wind in southern hemisphere would transport more water into the southern mesosphere if assuming there is equal water at lower heights in both hemisphere. The hemispheric difference in water vapor would be the combination result of all these factors.

[31] The hemispheric difference in available water content could explain the apparent differences in PMSE occurrence between two hemispheres [Balsley et al., 1995]. Usually the weaker PMSE in southern hemisphere is interpreted as the result of warmer mesopause. However, the TIME-GCM model predicts a colder mesopause in southern hemisphere as shown in Figure 10a. Now we

could explain the PMSE difference from the viewpoint of available water vapor. The lesser available water content in the south would cause the small ice particles, presumably responsible for PMSE, to have less surface area, and thus less capability to soak up free electrons, which causes an increase in the electron diffusivity. Therefore, even if the mesopause were colder in the south, the smaller water content would offset the greater nucleation rate, thus result in weaker PMSE in southern hemisphere. We are aware that the above water vapor results in Figure 11 and Figure 12 are from TIME-GCM model simulations. Observational data are needed to verify the model predictions.

[32] Thomas and Olivero [1989] found significant interannual variability in PMC summed frequencies on the order of 15% due to an unknown cause, but no consistent year-to-year trends. A significant trend in PMC occurrence frequency and brightness versus solar activity was found by examining long-term satellite data sets [Thomas et al., 1991; Thomas, 1995]. Maximum occurrence frequency and brightest PMC appeared during solar minimum conditions, which suggests an anti-correlation of PMC activity with solar activity. As explained in the previous section, the increased solar flux causes a dynamic adjustment that results in higher altitudes for both the mesopause and supersaturation regions. Since PMC mainly develop in supersaturation regions, we would expect higher PMC altitudes in the seasons with more solar flux. Higher saturation region would also contain less water vapor, thus results in lower PMC brightness and lower PMC occurrence frequency. Therefore, PMC with higher altitude but smaller brightness and occurrence frequency would be expected in the seasons with more solar flux.

## 7. Conclusions

[33] In summary, PMC were observed by an Fe Boltzmann temperature lidar at the South Pole in the 1999–2000 and 2000–2001 austral summer seasons. The interannual,

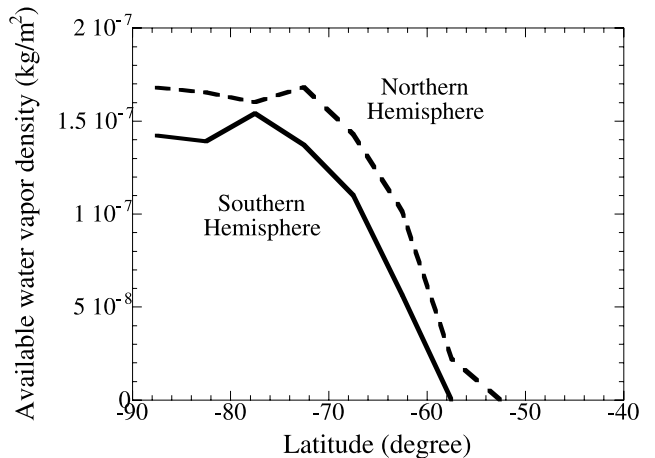


**Figure 12.** Integrated available water vapor density versus latitude on 13 days after summer solstice predicted by TIME-GCM in the southern hemisphere (solid line) and in the northern hemisphere (dashed line).

seasonal and diurnal variations of PMC were studied from more than 430 h data obtained during these two seasons. The most significant differences between the two seasons are that the mean total backscatter coefficient of PMC in the 2000–2001 season is 82% larger than in the 1999–2000 season, and the mean centroid altitude of PMC in the 2000–2001 season is 0.83 km lower than in the 1999–2000 season. Both seasons exhibit similar overall occurrence probabilities as about 67%. The overall mean peak backscatter ratio, mean peak volume backscatter coefficient and mean total backscatter coefficient of PMC in 1999–2000 and 2000–2001 seasons at the South Pole are  $58.4 \pm 1.5$ ,  $(3.75 \pm 0.10) \times 10^{-9} \text{ m}^{-1} \text{ sr}^{-1}$  and  $(5.45 \pm 0.19) \times 10^{-6} \text{ sr}^{-1}$ , respectively. The mean altitude of PMC in two seasons is  $85.03 \pm 0.05$  km, which is consistently 2–3 km higher than PMC observed in the northern hemisphere. The mean RMS width of PMC layer is  $0.75 \pm 0.02$  km. Clear seasonal variations of PMC altitudes were observed at the South Pole where they reached maximum altitude around 10–20 days after summer solstice. Seasonal variations of PMC backscatter coefficient and occurrence probability were also observed at the South Pole. Both reach maximum around 25–40 days after the summer solstice, and the PMC are brighter when the occurrence probability is higher. The South Pole PMC exhibit strong diurnal and semidiurnal variations in backscatter coefficient and centroid altitude. Both in-phase and out-of-phase relationships between PMC backscatter coefficient and centroid altitude were observed at the South Pole. The distribution of PMC backscatter coefficient versus altitude is roughly symmetric at the South Pole, and the largest backscatter coefficient occurs near the center of the altitude distribution around 85 km.

[34] Comparing lidar PMC observational data with the TIME-GCM data, we attribute the hemispheric difference in PMC altitude to the hemispheric differences in the supersaturation region altitudes and in the upwelling vertical wind. These differences are mainly caused by different solar forcing in two hemispheres that the solar flux in January is 6% greater than the solar flux in July because of the Earth's orbital eccentricity where the Earth is closest to the Sun on 3 January and farthest from the Sun on 5 July. Besides solar forcing, gravity wave forcing also contributes to the hemispheric difference and interannual difference. The interannual differences in PMC altitude and brightness are probably related to gravity wave and planetary wave variability. These results indicate the need for further measurement and modeling efforts to better understand the complex dynamic, chemical and microphysical processes operating in the cold summer mesopause region.

## Appendix A: Definitions and Equations for PMC Parameter Computation

[35] In the PMC region, the lidar receives backscattered photons from air molecules, PMC particles, and solar scattering photons as described by the LIDAR equation

$$N_s(z) = \left( \frac{P_L \Delta t}{hc/\lambda} T_a \right) [\beta_R(z) + \beta_{PMC}(z)] \Delta z \left( T_a \frac{A_R}{z^2} \eta \right) + N_B \quad (\text{A1})$$

**Table A1.** Equations for PMC Parameter Computation

Backscatter ratio  $R(z)$ :

$$R(z) = \frac{\text{Total signal}(z)}{\text{Molecular signal}(z)} = \frac{\beta_{PMC}(z) + \beta_R(z)}{\beta_R(z)} \quad (\text{A4})$$

$$R(z) = \frac{[N_s(z) - N_B] \cdot z^2}{[N_R(z_R) - N_B] \cdot z_R^2} \cdot \frac{n_R(z_R)}{n_R(z)} \quad (\text{A5})$$

Volume backscatter coefficient  $\beta(z)$ , i.e.,  $\beta_{PMC}(z)$ :

$$\beta_{PMC}(z) = \left[ \frac{[N_s(z) - N_B] \cdot z^2}{[N_R(z_R) - N_B] \cdot z_R^2} \cdot \frac{n_R(z)}{n_R(z_R)} \right] \beta_R(z_R) \quad (\text{A6})$$

$$\beta_R(z_R, \pi) = 2.938 \times 10^{-32} \frac{P(z_R)}{T(z_R)} \cdot \frac{1}{\lambda^{4.0117}} \quad (\text{A7})$$

Total backscatter coefficient  $\beta_{\text{Total}}$ :

$$\beta_{\text{Total}} = \int \beta_{PMC}(z, \pi) dz \quad (\text{A8})$$

Centroid altitude  $Z_C$ :

$$Z_C = \frac{\sum_i z_i \cdot \beta_{PMC}(z_i)}{\sum_i \beta_{PMC}(z_i)} \quad (\text{A9})$$

RMS width  $\sigma_{rms}$ :

$$\sigma_{rms} = \sqrt{\frac{\sum_i (z_i - Z_C)^2 \cdot \beta_{PMC}(z_i)}{\sum_i \beta_{PMC}(z_i)}} \quad (\text{A10})$$

At Rayleigh normalization altitude  $z_R$ , photon counts received by lidar are

$$N_R(z_R) = \left( \frac{P_L \Delta t}{hc/\lambda} T_a \right) \beta_R(z_R) \cdot \Delta z \cdot \left( T_a \cdot \frac{A_R}{z_R^2} \cdot \eta \right) + N_B \quad (\text{A2})$$

$\beta_R$  and  $\beta_{PMC}$  represent the volume backscatter coefficient for air molecule (Rayleigh) scattering and PMC particle (Mie) scattering.

[36] The ratio of Rayleigh angular volume backscatter coefficients at altitude  $z_R$  and  $z$  is

$$\frac{\beta_R(z_R)}{\beta_R(z)} = \frac{n_R(z_R) \cdot \sigma_R(z_R)}{n_R(z) \cdot \sigma_R(z)} = \frac{n_R(z_R)}{n_R(z)} \quad (\text{A3})$$

assuming Rayleigh backscatter cross sections  $\sigma_R(z_R) = \sigma_R(z)$ . Here,  $n_R(z)$  and  $n_R(z_R)$  are the atmosphere molecule number density at PMC altitude  $z$  and Rayleigh normalization altitude  $z_R$ .

[37] Therefore, the PMC parameters are defined and calculated as shown in Table A1.

## Notation

$N_s(z)$	= expected photon counts at PMC altitude $z$
$N_R(z_R)$	= expected photon counts at Rayleigh scattering altitude $z_R$
$P_L$	= laser output power
$\Delta t$	= integration time
$h$	= Plank constant
$c$	= light speed
$\lambda$	= laser wavelength
$T_a$	= one-way transmittance of lower atmosphere at wavelength $\lambda$
$\Delta z$	= integrate altitude range
$\eta$	= lidar optical efficiency
$N_B$	= background photon counts due to solar scattering and detector dark count
$A_R$	= receiving telescope aperture area
$\beta(z)$	= angular volume backscatter coefficient, i.e., angular volume scattering coefficient at $\theta = \pi$
$P(z_R)$	= atmospheric pressure at $z_R$ (mbar)
$T(z_R)$	= atmospheric temperature at $z_R$ (K).

## Appendix B: TIME-GCM Simulations

[38] The South Pole lidar observations have shown a higher altitude of polar mesospheric clouds (PMC) than in the North Pole region. In an attempt to understand possible causes for these differences, numerical simulations with the NCAR Thermosphere-Ionosphere-Mesosphere-Electrodynamics General Circulation Model (TIME-GCM) were made to suggest possible physical mechanism that could cause such differences. There are many processes responsible for the structure of the mesopause region and so it is difficult to suggest any one processes without adequate measurements to quantify all possible sources. Therefore, in this appendix we discuss a few of the possible mechanisms that may contribute to the observations that the South Pole PMC appear to be higher in altitude during the austral summers of 1999–2000 and 2000–2001 than the PMC in the northern hemisphere during the summer of 1999.

[39] The NCAR TIME-GCM is the latest in a series of three-dimensional time-dependent models that have been developed over the past two decades to simulate the circulation, temperature, and compositional structure of the upper atmosphere and ionosphere. It combines all of the features of the TGCM [Dickinson *et al.*, 1981, 1984], TIGCM [Roble *et al.*, 1988], and TIE-GCM [Richmond *et al.*, 1992] and the model has been extended downward to 30 km altitude including aeronomical processes appropriate for the mesosphere and upper stratosphere, as described by Roble and Ridley [1994], Roble *et al.* [1987], and Roble [1995]. The most recent aeronomical updates to these original papers are given by Roble [2000].

[40] The TIME-GCM was used to simulate a yearlong run as described by Roble [2000]. In preparation for this yearlong run the TIME-GCM was used first to simulate a perpetual March equinox and December solstice for solar cycle medium conditions appropriate to the time of Upper Atmosphere Research Satellite (UARS) measurements during the March/April and December/January 1992/1993 periods as described by McLandress *et al.* [1996]. Although perpetual March equinox and December solstice simulations may not

be realistic because of changing seasons, they are consistent approximations when compared with the binned UARS data that span a two month period. This time period was needed to retrieve the diurnal cycle because of the slow UARS orbital precession as discussed by McLandress *et al.* [1996].

[41] For the model simulations a daily and 3 month time averaged solar F10.7 flux value of 150 was used to specify the solar spectral irradiance in the solar EUV and UV flux model embedded within the TIME-GCM [Roble, 1995]. A steady auroral forcing with ionospheric convection specified by a 45 kV cross-polar cap potential drop and auroral particle precipitation hemispheric power input of 6 GW was used in the auroral model described by Roble and Ridley [1987].

[42] The gravity wave forcing at the lower boundary is similar to that used by Garcia and Solomon [1985] having a latitudinal distribution of  $\cos(2L)$  where  $L$  is latitude. The gravity wave model is based on the parameterizations of Lindzen [1981] and modified by Kiehl *et al.* [1998]. The TIME-GCM has a lower boundary at 10 hPa (30 km) and the assumed gravity wave forcing at the lower boundary is symmetrical with respect to season for the yearlong run, as described by Roble [2000]. A detailed description of the Gravity Wave Parameterization used in the TIME-GCM is given on pages 96–103 in the work of Kiehl *et al.* [1996]. Since the model does not include a troposphere or lower stratosphere there is no consideration of wave filtering below 30 km in this simplified simulation. Therefore, there is no difference in the seasonal variation of gravity wave forcing between the northern or southern hemisphere due to wind filtering below 30 km and the only differences at mesospheric heights would be due to wind filtering above 30 km within the model. Six waves were used in each of the cardinal directions with a 20 m/s offset in the eastward direction, consistent with the findings of Medvedev *et al.* [1998].

[43] With these boundary conditions and specified inputs for the parameterizations all other physical and chemical processes are calculated self-consistently. For example, heating rates are calculated using the calculated ozone distribution and the amount of solar energy absorbed at each grid point and time step. Similarly IR cooling is determined using the calculated CO<sub>2</sub> and O distributions as well as model calculated temperatures.

[44] With the equinox and solstice simulation parameters established and constrained by the UARS data, the TIME-GCM was then run to simulate a seasonal variation during the year. For this year's simulation the solar and auroral forcing were held constant at the values discussed above, therefore, the calculated variation of temperature, winds, and composition are due entirely to the seasonal variation of solar forcing. The model also included a 6% solar flux variation caused by the Earth's orbital eccentricity. This variation has been shown by Bouger *et al.* [2000] to be important for hemispherical differences between thermospheric and ionospheric structure and dynamics. The derived parameters, such as the gravity wave forcings from the above UARS studies, were allowed to vary sinusoidally between the equinox and solstice conditions and were symmetrical between hemispheres. At the lower boundary the tidal forcing from the lower atmosphere was held fixed during the year and only the zonally averaged latitudinal gradients of geopotential and temperature were allowed to vary in accordance with the variations specified by the

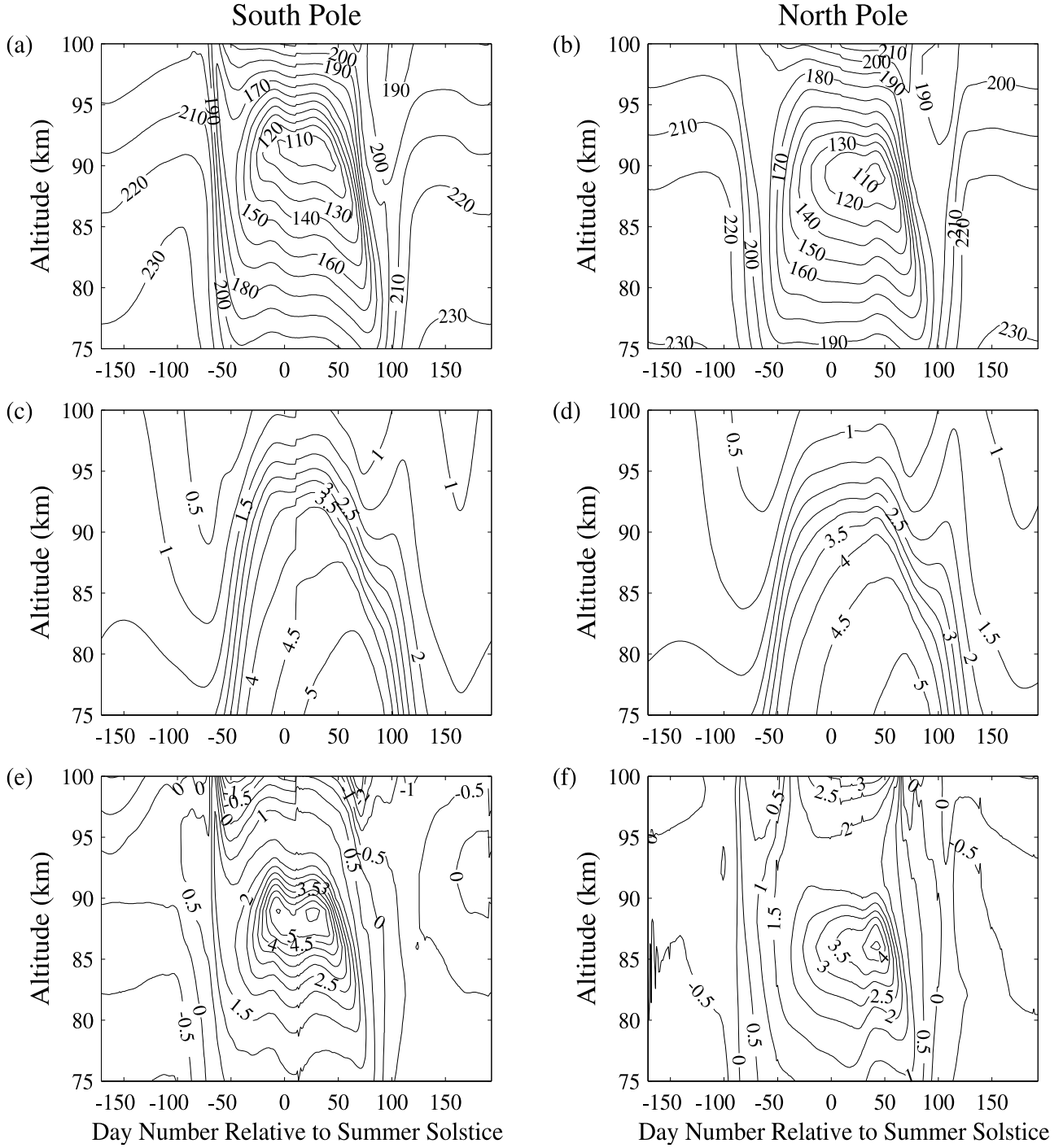


**Figure 13.** Some basic results from the yearlong run TIME-GCM simulation at the South and North Poles: (a, b) Neutral temperature (K); (c, d) Water vapor mixing ratio (ppmv); (e, f) Vertical wind (cm/s).

Flemming et al. [1988] climatological model at 10 mb. Model histories were recorded daily at 00 UT and hourly histories for certain fields were obtained every 10 days throughout the year. Results and overall performance of the model have been discussed by Roble [2000].

[45] Thus, for this yearlong run of the model, the only differences between the northern and southern hemisphere external forcing are due to the seasonal variation of the Sun, the 6% eccentricity variation and hemispherical differences of lower boundary forcing as specified by the empirical

model. There are also differences in the Earth's geomagnetic field but these mainly affect the thermosphere and ionosphere above about 100 km. All other physical and chemical processes were symmetrical between hemispheres.

[46] The results of the simulation have been discussed in the text of this paper for the north and south polar region. Plotted in Figure 13 are some basic output of the yearlong run TIME-GCM simulations: the variations of neutral temperatures, water vapor mixing ratio and vertical wind versus altitude and day number at the South and North

Poles. A close examination of the height of the mesopause at both poles showed that it was greater by a few kilometers during southern hemisphere summer than in northern hemisphere summer. Figure 10 shows an example of the vertical profiles of temperature and vertical wind at the South and North Poles on the 13th day after summer solstice. The South Pole mesopause is about 2 km higher than the North Pole mesopause. This feature was then examined in detail and it was found that the increased solar heating due to the Earth's orbital eccentricity contributed about 1 km to the observed difference. This indicates that other processes may also be involved, such as differences in gravity wave forcing, planetary waves, etc.

[47] The model calculations showed that the southern hemisphere summer stratopause temperature is warmer than the northern hemisphere summer stratopause temperature by about 5 K primarily because the Earth is closer to the Sun in January than in July. Similar differences occur in other fields, such as ozone and atomic oxygen indicating higher photodissociation rates in southern hemisphere summer. It also occurs in the model calculated solar heating rate being larger in January than July. The increased solar heating causes a dynamic response that results in a higher mesopause altitude in January than July. The greater heating also results in larger vertical wind velocities with colder temperatures and higher mesopause altitudes in the southern hemisphere summer consistent with the data.

[48] In addition to the above there are also differences caused by interhemisphere differences of lower boundary geopotential and temperature forcings. The stratospheric zonal wind jets are about 10 m/s stronger in the southern summer than the northern summer and these changes alter the characteristics of the parameterized gravity wave momentum flux such that the zonal momentum forcing at the high latitude summer mesopause is about 40 m/s/day larger and about 2 km higher in the southern summer mesopause than in the northern summer mesopause. The mesopause meridional winds are also a few m/s stronger in the summer southern hemisphere.

[49] Thus, in the yearlong run of the TIME-GCM, the reason for the higher summer mesopause in the southern hemisphere is the increased heating and photodissociation when the Earth is closer to the Sun in January and differences in gravity wave momentum deposition. In the year-long run, the gravity wave flux at the lower boundary of the model are the same for both the north and south polar region. However, the zonally averaged geopotential from the empirical model is not symmetric between the North and South Poles and this may contribute to differences in gravity wave transmission and momentum deposition. These differences along with eccentricity altered solar forcing combine to give the good agreement of the model simulation with lidar PMC data.

[50] To examine the influence of orbital eccentricity alone on the structure and dynamics of the mesosphere and lower thermosphere in more detail, identical model runs were made with the TIME-GCM for perpetual December solstice conditions where the only difference was that the solar flux used in the model was increased 3% for one run and decreased 3% for the second run. Nothing else was changed—gravity wave forcing, lower boundary gradients, aurora precipitation, cross-polar cap potential drop etc. were

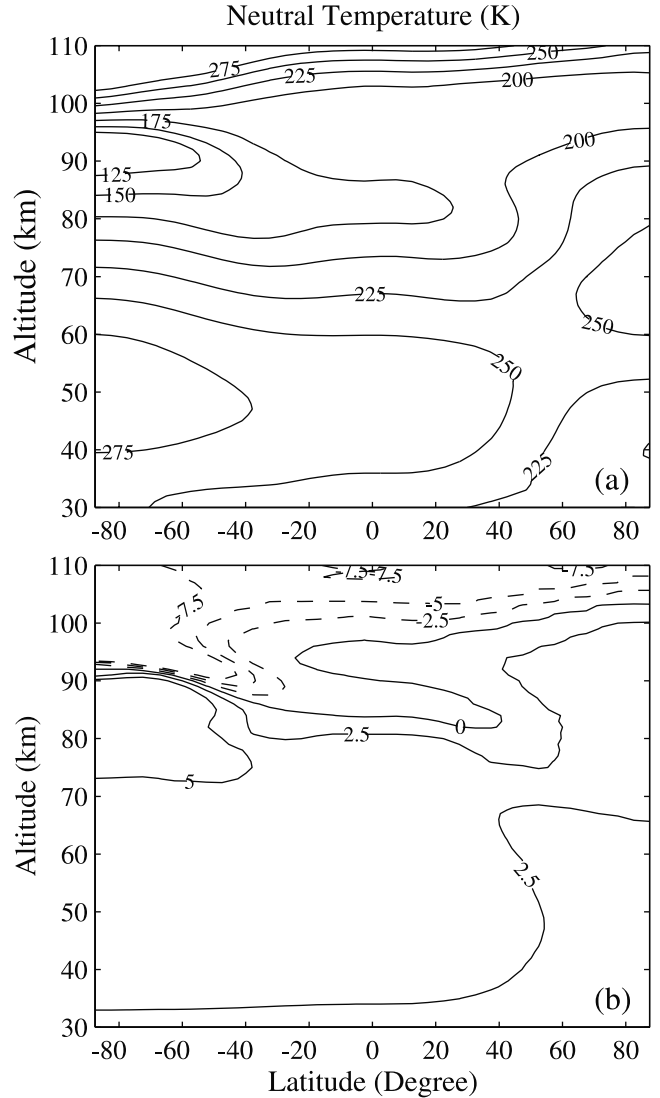


**Figure 14.** TIME-GCM simulation for perpetual December solstice conditions: neutral temperature (K)—(a) total field, (b) difference field.

all held constant. The model was run for 30 days, sufficient for most dynamic processes in the mesosphere and thermosphere to adjust. Experiments show that 15 days are generally sufficient for most processes except for long-lived chemical species with slow dissociation rates.

[51] The model runs were made using the TIME-GCM with 4 grid points per scale height vertical resolution. The calculated total and difference field for several fields are shown in the accompanying figures. Here, the total field is referred to the case with 3% increase of solar flux, and the difference field means the difference between the case with the 3% solar flux increase minus the 3% decrease. The main differences are discussed below:

[52] Figure 14a shows the calculated total temperature (i.e., the temperature for the case with 3% increase of solar flux) for December solstice and Figure 14b shows the temperature difference between the cases with the 3% increase minus the 3% decrease. The lower boundary temperatures differences are zero. Above the boundary the calculated

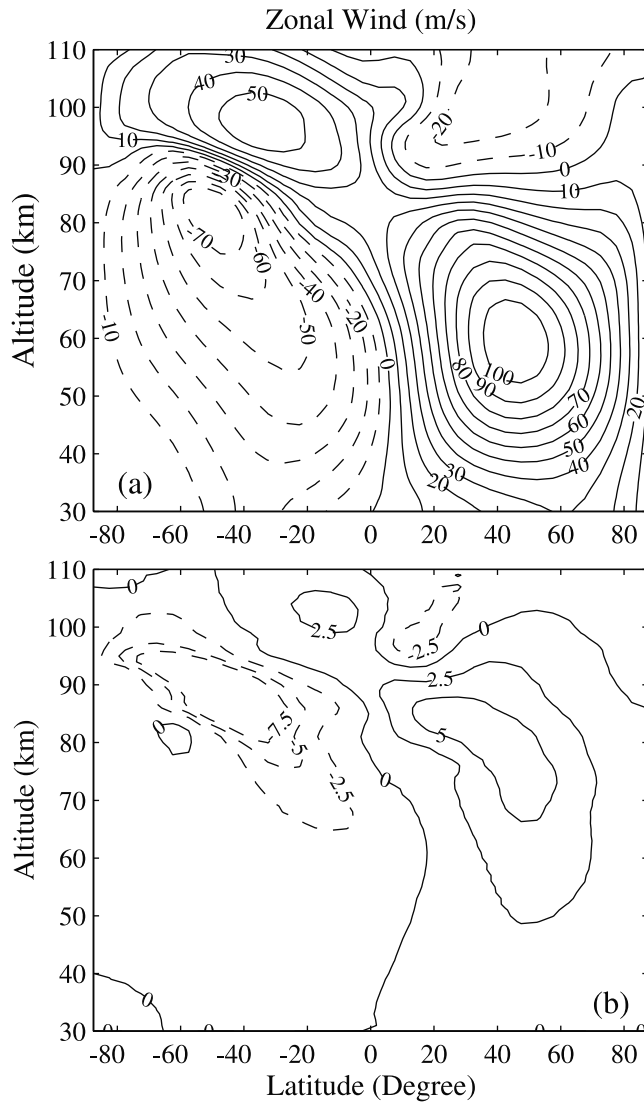


**Figure 15.** TIME-GCM simulation for perpetual December solstice conditions: zonal wind (m/s)—(a) total field, (b) difference field.

temperature at the South Pole increases to about 4 K at 60 km and to 6.5 K at 85 km. At the mesopause, the temperature decreases with altitude because the constant pressure surface for the case with the higher solar flux is at a higher altitude and against the positive temperature gradient above the mesopause. The temperature of lower solar flux case is larger than the higher solar flux case at a given altitude above the mesopause.

[53] Figure 15a shows the calculated zonal wind for December solstice and Figure 15b shows the zonal wind differences between the two cases described above. The change in solar flux affects the zonal winds and this affects the gravity wave transmission and energy and momentum deposition. These changes, however, are all solar induced and so the whole mesosphere and thermosphere is altered. In the southern hemisphere the difference zonal winds are westward and they are eastward in the northern hemisphere at velocities peaking near 45 degrees latitude and 85 km altitude. The difference winds are small below 60 km ( $\sim 1$  m/s).

[54] Figures 16a and 16b are similar but for the meridional wind. The difference meridional wind response is mainly in the summer mesopause region and the winds are southward below 90 km and northward above 90 km with zonal mean velocities of about 2–3 m/s.

[55] Figures 17a and 17b are similar but for the vertical wind. The difference vertical wind is upward in the South Pole region above 90 km and downward below at velocities of 3 mm/s. This is a consequence of the reversed circulation cell in the lower thermosphere as shown in the plot of the mass flow stream function shown in Figure 18.

[56] Finally, the line plot in Figure 19 is the height difference of constant pressure surfaces between the two cases indicating that the mesopause is about 0.8 km higher during the increased solar flux compared to the decreased solar flux case.

[57] In summary, the simulation that shows the higher mesopause is based on a full dynamic response of the model to differences in solar heating. That is the only parameter

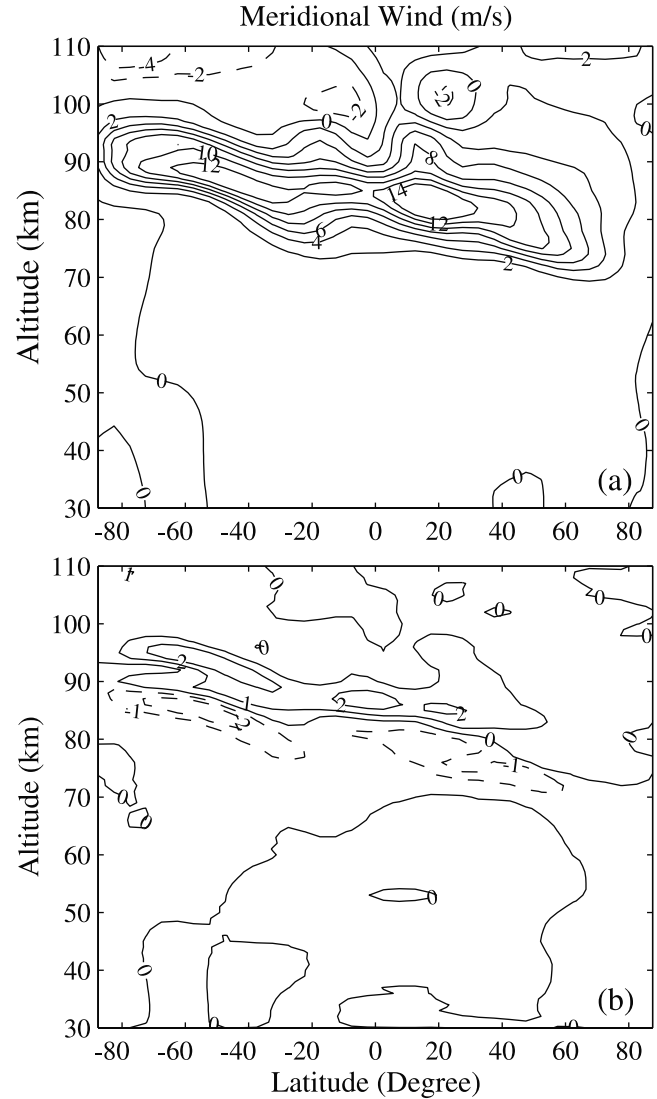


**Figure 16.** TIME-GCM simulation for perpetual December solstice conditions: meridional wind (m/s)—(a) total field, (b) difference field.

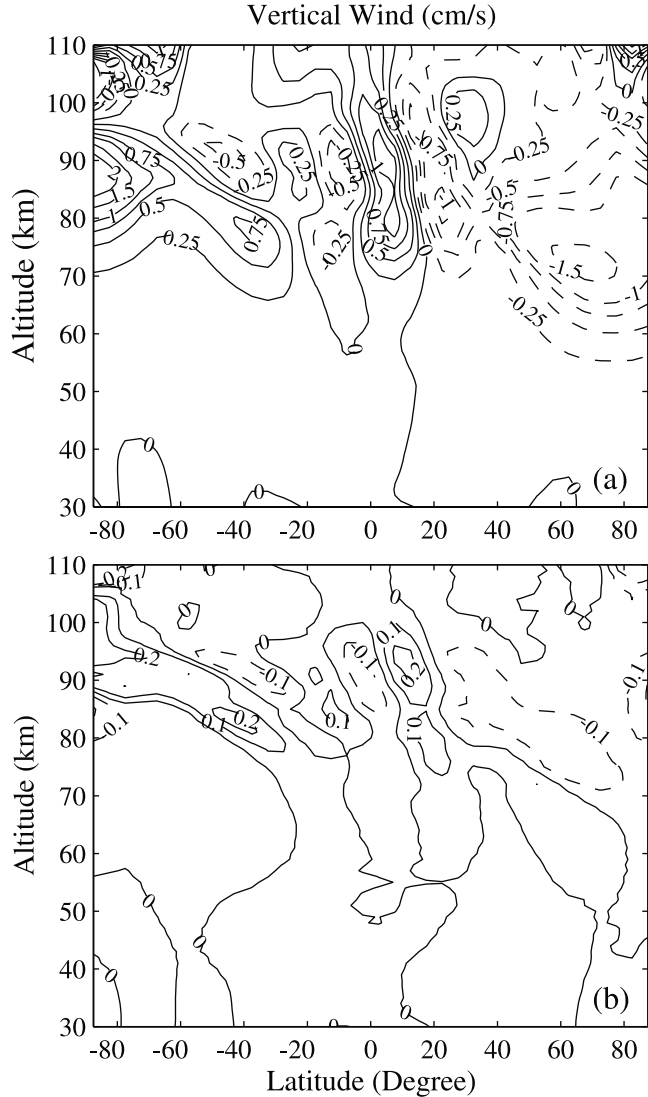


**Figure 17.** TIME-GCM simulation for perpetual December solstice conditions: vertical wind (cm/s)—(a) total field, (b) difference field.

that has been changed and all other physical and chemical processes are calculated self-consistently. These results suggest that part of the observed height difference is due to orbital eccentricity and part by changes in the gravity wave transmission. This when combined with the lower boundary geopotential gradient differences in the empirical model that further influences the gravity wave transmission and momentum deposition are the combined physical mechanisms in the TIME-GCM that are identified as being able to account for the good agreement between model calculations and the lidar PMC data.

### Appendix C: Derivation of the Force Balance Equation (2) for PMC Altitude

[58] According to the explanation in the appendix of [Reid, 1975], the terminal speed of small particles in the atmosphere is determined in part by the ratio of the mean free path of the air molecules to some characteristic linear dimension of the particles. In the mesopause region, the

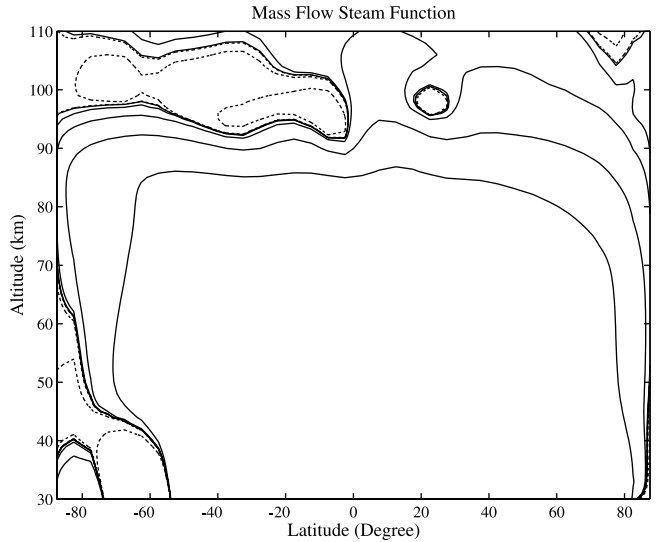


**Figure 18.** TIME-GCM simulation for perpetual December solstice conditions: an illustration of the mass flow steam function. Positive contours (solid lines) are clockwise and negative (dashed lines) are counter clockwise with a mass flow between contours of about  $10^7$  gm/s.

mean free path is of the order of 1 cm ( $10^{-2}$  m), and the size of PMC particles is about  $10-100$  nm ( $10^{-8}-10^{-7}$  m). Thus, the interaction between individual molecules can be neglected for scale lengths comparable with the particle size. Under these conditions, the terminal fallspeed is determined by the force balance between the net upward force and the downward gravitational force on the particle. This net upward force is due to the difference in velocity between the molecules striking the particle from below and those striking the particle from above.

[59] Reid [1975] only considered the case without upwelling vertical wind. We consider the case with upwelling vertical wind here. Using the same symbol as Reid, when there is no upwelling vertical wind, the atmosphere molecule velocity is  $\vec{u}$  relative to the ground. When there is upwelling vertical wind velocity  $\vec{w}$  (relative to the ground),

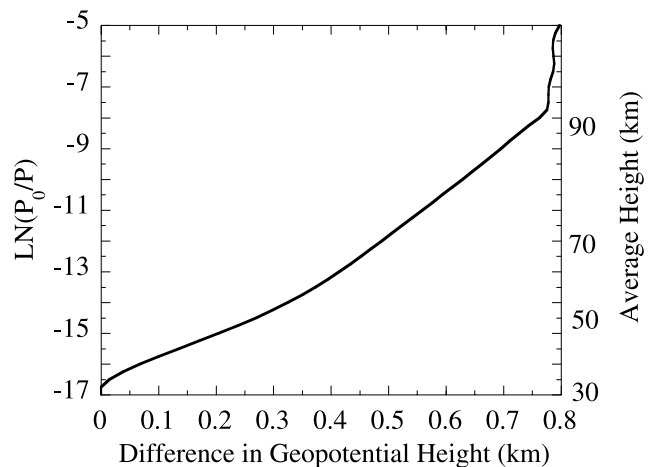


**Figure 19.** TIME-GCM simulation for perpetual December solstice conditions: the height difference of constant pressure surfaces between the two cases.

the molecule velocity relative to the ground will be  $\vec{u} + \vec{w}$ . Assume the PMC particle has a vertical falling velocity  $\vec{v}$  relative to the ground and an elementary area  $dA$ , which surface is normal to  $\vec{v}$ . So the velocity of molecule relative to the PMC particle (i.e., in the rest frame of the particle) is given by  $\vec{u}' = \vec{u} + \vec{w} - \vec{v}$ . Assume the molecule velocity  $\vec{u}$  strikes the particle at an angle  $\theta$ . For the molecule strikes the lower face of the particle (i.e., the molecule moves upward), the apparent speed is

$$u' = u^2 + (w + v)^2 + 2u(w + v) \cos \theta \quad (C1)$$

For the molecule strikes the upper face of the particle (i.e., the molecule moves downward), the apparent speed is

$$u' = u^2 + (w + v)^2 - 2u(w + v) \cos \theta \quad (C2)$$

where  $u'$ ,  $u$ ,  $v$  and  $w$  are all positive speed. The apparent angle of approach for the latter one is

$$\sin \varphi = \frac{u}{u'} \sin \theta, \cos \varphi = \frac{u \cos \theta - (w + v)}{u'} \quad (C3)$$

[60] Take a cylinder of length  $u'$  based on the upper face of the elementary area and inclined at an angle  $\varphi$  to the vertical. The number of molecules with speeds between  $u$  and  $u + du$  in this cylinder is  $N(u)u' \cos \varphi dudA$ , where  $N(u)du$  is the molecule number density. These molecules move in all directions isotropically, and a fraction  $\frac{1}{2}\sin \theta d\theta$  will be travelling toward the particle from an elementary strip of area  $2\pi \sin \theta d\theta$ , and will strike the particle in 1 s. Thus the number of impacts from the upper face per second is  $\frac{1}{2}N(u)u' \cos \varphi \sin \theta d\theta dudA$ . Since the molecule's normal velocity component is reversed after impact, each such impact will provide an impulse  $2m_a u' \cos \varphi$ , where  $m_a$  is the mass of an air molecule. Thus, the downward force contributed by these molecules is

$$dF_{dn} = N(u)m_a u'^2 \cos^2 \varphi \sin \theta dudAd\theta. \quad (C4)$$

By integrating over the entire upper hemisphere from  $\theta = 0$  to  $\theta = \pi/2$  and using (C2) and (C3), we have the downward force due to molecules with speeds in the range  $[u, u + du]$  as

$$\Delta F_{dn} = N(u)m_a \left[ \frac{u^2}{3} + (w + v)^2 - u(w + v) \right] dudA. \quad (C5)$$

The upward force over the lower face of the particle can be found in the similar way combining with equation (C1) as

$$\Delta F_{up} = N(u)m_a \left[ \frac{u^2}{3} + (w + v)^2 + u(w + v) \right] dudA. \quad (C6)$$

The net upward force on the elementary area is obtained by subtracting equation (C5) from equation (C6):

$$\Delta F = 2N(u)m_a u(w + v)dudA. \quad (C7)$$

We assume that the distribution of air molecule speed is given by a Maxwellian distribution at temperature  $T$ :

$$N(u)du = 4\pi n u^2 \left( \frac{m_a}{2\pi kT} \right)^{3/2} \exp \left( -\frac{m_a u^2}{2kT} \right) du \quad (C8)$$

where  $n$  is the total number density of air molecules with all kind of speeds, and  $k$  is Boltzmann constant. Substituting equation (C8) into equation (C7) and integrating over all speeds from zero to infinity, we have the net upward force on the elementary area  $dA$

$$F = 4n(w + v) \left( \frac{2m_a kT}{\pi} \right)^{1/2} dA. \quad (C9)$$

For the more general case in which the elementary area  $dA$  is inclined at an arbitrary angle  $\gamma$  to the horizontal, we use the same way as [Reid, 1975] and get the net upward vertical force as

$$F = 4n(w + v) \left( \frac{2m_a kT}{\pi} \right)^{1/2} \cos^2 \gamma dA. \quad (C10)$$

The total upward force on the whole particle is obtained by integrating over the surface area of the particle

$$F_{Total} = 4n(w + v) \left( \frac{2m_a kT}{\pi} \right)^{1/2} \int \cos^2 \gamma dA. \quad (C11)$$

The terminal fallspeed of the particle is reached when this net upward force exactly balances the downward gravitational force on the particle:

$$4n(w + v) \left( \frac{2m_a kT}{\pi} \right)^{1/2} \int \cos^2 \gamma dA = mg \quad (C12)$$

where  $m$  is the mass of PMC particle and  $g$  is the gravity acceleration. So the terminal fallspeed of PMC particle is

$$v = \frac{mg - 4nw \left( \frac{2m_a kT}{\pi} \right)^{1/2} \int \cos^2 \gamma dA}{4n \left( \frac{2m_a kT}{\pi} \right)^{1/2} \int \cos^2 \gamma dA} \quad (C13)$$

[61] When the terminal fallspeed is equal to zero, the PMC particle will stay and be observed at that altitude. Therefore, the PMC altitude will be determined by the following equation ( $v = 0$ ):

$$mg = 4nw \left( \frac{2m_a kT}{\pi} \right)^{1/2} \int \cos^2 \gamma dA \quad (C14)$$

Let

$$C = 4 \left( \frac{2kT}{\pi m_a} \right)^{1/2} \int \cos^2 \gamma dA, \quad (C15)$$

then equation (C14) can be simplified to

$$mg = C\rho w \quad (C16)$$

where the atmosphere mass density  $\rho = m_a n$ , and  $C$  is the drag coefficient. Equation (C16) is the same force balance equation as equation (2) in the text. The right hand-side of

equation (C16) represents the upwelling force due to the atmosphere upwelling vertical wind.

[62] **Acknowledgments.** This development, deployment, and operation of the University of Illinois Fe lidar at South Pole were supported by the National Science Foundation grants NSF ATM 96-12251 and NSF OPP 96-16664. The National Center for Atmospheric Research is sponsored by the National Science Foundation.

## References

- Alpers, M., M. Gerding, J. Höffner, and U. von Zahn, NLC particle properties from a five-color lidar observation at 54°N, *J. Geophys. Res.*, **105**, 12,235–12,240, 2000.
- Avaste, O., Noctilucent clouds, *J. Atmos. Terr. Phys.*, **55**, 133–143, 1993.
- Backhouse, T. W., The luminous cirrus clouds of June and July, *Meteorol. Mag.*, **20**, 133, 1985.
- Balsley, B. B., R. F. Woodman, M. Sarango, R. Rodriguez, J. Urbina, E. Ragaini, J. Carey, M. Huaman, and A. Giraldez, On the lack of southern hemisphere polar mesosphere summer echoes, *J. Geophys. Res.*, **100**, 11,685–11,693, 1995.
- Bougher, S. W., S. Engel, R. G. Roble, and B. Foster, Comparative terrestrial planet thermospheres, 3, Solar cycle variation of global structure and winds at Solstices, *J. Geophys. Res.*, **105**, 17,669–17,692, 2000.
- Carbary, J. F., G. J. Romick, D. Morrison, L. J. Paxton, and C. I. Meng, Altitudes of polar mesospheric clouds observed by a middle ultraviolet imager, *J. Geophys. Res.*, **104**, 10,089–10,100, 1999.
- Carbary, J. F., D. Morrison, and G. J. Romick, Hemispheric comparison of PMC altitudes, *Geophys. Res. Lett.*, **28**, 725–728, 2001a.
- Carbary, J. F., D. Morrison, and G. J. Romick, Latitude variations in light scattered from polar mesospheric clouds, *Geophys. Res. Lett.*, **28**, 2605–2608, 2001b.
- Chapman, S., and P. C. Kendall, Noctilucent clouds and thermospheric dust: Their diffusion and height distribution, *Q. J. R. Meteorol. Soc.*, **91**, 115–131, 1965.
- Charlson, R. J., Noctilucent clouds: A steady-state model, *Q. J. R. Meteorol. Soc.*, **91**, 517–523, 1965.
- Charlson, R. J., A simple noctilucent cloud model, *Tellus*, **18**, 451, 1966.
- Chu, X., C. S. Gardner, and G. Papen, Lidar observations of polar mesospheric clouds at South Pole: Seasonal variations, *Geophys. Res. Lett.*, **28**, 1203–1206, 2001a.
- Chu, X., C. S. Gardner, and G. Papen, Lidar observations of polar mesospheric clouds at South Pole: Diurnal variations, *Geophys. Res. Lett.*, **28**, 1937–1940, 2001b.
- Chu, X., W. Pan, G. Papen, C. S. Gardner, and J. Gelbwachs, Fe Boltzmann temperature lidar: Design, error analysis, and initial results at the North and South Poles, *Appl. Opt.*, **41**, 4400–4410, 2002.
- Debrechtian, D. J., et al., An analysis of POAMII solar occultation observations of polar mesospheric clouds in the southern hemisphere, *J. Geophys. Res.*, **102**, 1971–1981, 1997.
- Dickinson, R. E., E. C. Ridley, and R. G. Roble, A three-dimensional general circulation model of the thermosphere, *J. Geophys. Res.*, **86**, 1499–1512, 1981.
- Dickinson, R. E., E. C. Ridley, and R. G. Roble, Thermospheric general circulation with coupled dynamics and composition, *J. Atmos. Sci.*, **41**, 205–219, 1984.
- Donahue, T. M., B. Guenther, and J. E. Blamont, Noctilucent clouds in daytime: Circumpolar particulate layers near the summer mesopause, *J. Atmos. Sci.*, **29**, 1205–1209, 1972.
- Dowdy, A., R. A. Vincent, K. Igarashi, Y. Murayama, and D. J. Murphy, A comparison of mean winds and gravity wave activity in the northern and southern polar MLT, *Geophys. Res. Lett.*, **28**, 1475–1478, 2001.
- Evans, W. F., L. R. Lafframboise, K. R. Sine, R. H. Wiens, and G. G. Shepherd, Observation of polar mesospheric clouds in summer, 1993 by the WINDII instrument on UARS, *Geophys. Res. Lett.*, **22**, 2793–2796, 1995.
- Flemming, E. L., S. Chandra, M. R. Schöberl, and J. J. Barnett, Monthly mean global climatology of temperature, wind, geopotential height, and pressure for 0–120 km, *NASA Tech. Memo TM-100697*, p. 85, Goddard Space Flight Cent., Greenbelt, Md., 1988.
- Gadsden, M., The silver-blue cloudlets again: Nucleation and growth of ice in the mesosphere, *Planet. Space Sci.*, **29**, 1079–1087, 1981.
- Gadsden, M., Polar mesospheric clouds seen from geostationary orbit, *J. Atmos. Sol. Terr. Phys.*, **62**, 31–36, 2000.
- Gadsden, M., and W. Schröder, *Noctilucent Clouds*, Springer-Verlag, New York, 1989.
- Garcia, R. R., Dynamics, radiation, and photochemistry in the mesosphere: Implications for the formation of noctilucent clouds, *J. Geophys. Res.*, **94**, 14,605–14,615, 1989.
- Garcia, R. R., and S. Solomon, The effect of breaking gravity waves on the dynamics and chemical composition of the mesosphere and lower thermosphere, *J. Geophys. Res.*, **90**, 3850–3868, 1985.
- Gardner, C. S., G. C. Papen, X. Chu, and W. Pan, First lidar observations of middle atmosphere temperatures, Fe densities, and polar mesospheric clouds over the North and South poles, *Geophys. Res. Lett.*, **28**, 1199–1202, 2001.
- Gumbel, J., and G. Witt, In situ measurements of the vertical structure of a noctilucent cloud, *Geophys. Res. Lett.*, **25**, 493–496, 1998.
- Hansen, G., M. Serwazi, and U. von Zahn, First detection of a noctilucent cloud by lidar, *Geophys. Res. Lett.*, **16**, 1445–1448, 1989.
- Hervig, M., R. E. Thompson, M. McHugh, L. L. Gordley, J. M. Russell III, and M. E. Summers, First confirmation that water ice is the primary component of polar mesospheric clouds, *Geophys. Res. Lett.*, **28**, 971–974, 2001.
- Hessvedt, E., Note on the nature of noctilucent clouds, *J. Geophys. Res.*, **99**, 1985–1987, 1961.
- Hessvedt, E., On the possibility of ice cloud formation at the mesopause, *Tellus*, **290**–296, 1962.
- Huaman, M. M., and B. B. Balsley, Differences in near-mesopause summer winds, temperatures, and water vapor at northern and southern latitudes as possible causal factors for inter-hemispheric PMSE differences, *Geophys. Res. Lett.*, **26**, 1529–1532, 1999.
- Humphreys, W. J., Nacreous and noctilucent clouds, *Mon. Weather Rev.*, **61**, 228–229, 1933.
- Jensen, E., G. E. Thomas, and O. B. Toon, On the diurnal variation of noctilucent clouds, *J. Geophys. Res.*, **94**, 14,693–14,702, 1989.
- Jensen, E. J., and G. E. Thomas, A growth-sedimentation model of polar mesospheric clouds: Comparisons with SME measurements, *J. Geophys. Res.*, **93**, 2461–2473, 1988.
- Jensen, E. J., and G. E. Thomas, Numerical simulations of the effects of gravity waves on noctilucent clouds, *J. Geophys. Res.*, **99**, 3421–3430, 1994.
- Kiehl, J. T., J. J. Hack, G. B. Bonan, B. A. Boville, B. P. Briegleb, D. L. Williamson, and P. J. Rasch, Description of the NCAR Community Climate Model (CCM3), *NCAR Tech. Note*, NCAR/TN-420+STR, 1996.
- Kiehl, J. T., J. J. Hack, G. B. Bonan, B. A. Boville, D. L. Williamson, and P. J. Rasch, The National Center for Atmospheric Research Community Climate Model: CCM3, *J. Clim.*, **11**, 1131–1149, 1998.
- Klostermeyer, J., A simple model of the ice particle size distribution in noctilucent clouds, *J. Geophys. Res.*, **103**, 28,743–28,752, 1998.
- Klostermeyer, J., Effect of tidal variability on the mean diurnal variation of noctilucent clouds, *J. Geophys. Res.*, **106**, 9749–9755, 2001.
- Lindzen, R. S., Turbulence and stress owing to gravity wave and tidal breakdown, *J. Geophys. Res.*, **86**, 9707–9714, 1981.
- Lübken, F.-J., M. J. Jarvis, and G. O. L. Jones, First in situ temperature measurements at the Antarctic summer mesopause, *Geophys. Res. Lett.*, **26**, 3581–3584, 1999.
- McLandress, C., G. G. Shepherd, B. H. Solheim, M. D. Burrage, P. B. Hays, and W. R. Skinner, Combined mesosphere/thermosphere winds using WINDII and HRDI data from the Upper Atmosphere Research Satellite, *J. Geophys. Res.*, **101**, 10,441–10,453, 1996.
- Medvedev, A. S., G. P. Klaassen, and S. R. Beagley, On the role of an anisotropic gravity wave spectrum in maintaining the circulation of the middle atmosphere, *Geophys. Res. Lett.*, **25**, 509–512, 1998.
- Meriwether, J. W., R. Farley, R. McNutt, and P. D. Dao, Application of the Rayleigh lidar to observations of noctilucent clouds, *J. Geophys. Res.*, **98**, 14,979–14,989, 1993.
- Randel, W. J., Global Atmospheric Circulation Statistics, 1000–1mb, *NCAR Tech. Note*, NCAR/TN-366+STR, 1992.
- Reid, G. C., Ice clouds at the summer polar mesopause, *J. Atmos. Sci.*, **32**, 523–535, 1975.
- Richmond, A. D., E. C. Ridley, and R. G. Roble, A thermosphere/ionosphere general circulation model with coupled electrodynamics, *Geophys. Res. Lett.*, **19**, 601–604, 1992.
- Roble, R. G., Energetics of the mesosphere and thermosphere, in the upper mesosphere and lower thermosphere: A review of experiment and theory, *Geophys. Monogr.*, **87**, 1–21, 1995.
- Roble, R. G., On the feasibility of developing a global atmospheric model extending from the ground to the exosphere, *Geophys. Monogr.*, **123**, 53–67, 2000.
- Roble, R. G., and E. C. Ridley, A thermosphere-ionosphere-mesosphere-electrodynamics general circulation model (TIME-GCM): Equinox solar cycle minimum simulations (30–500 km), *Geophys. Res. Lett.*, **21**, 417–420, 1994.
- Roble, R. G., E. C. Ridley, and R. E. Dickinson, On the global mean structure of the thermosphere, *J. Geophys. Res.*, **92**, 8745–8758, 1987.
- Roble, R. G., E. C. Ridley, A. D. Richmond, and R. E. Dickinson, A coupled thermosphere/ionosphere general circulation model, *Geophys. Res. Lett.*, **15**, 1325–1328, 1988.

- Rottman, G., T. Woods, M. Snow, and G. DeToma, The solar cycle variation in ultraviolet irradiance, *Adv. Space Res.*, 27, 1927–1932, 2001.
- Schröder, W., Were noctilucent clouds caused by the Krakatoa eruption? A case study of the research problems before 1885, *Bull. Am. Meteorol. Soc.*, 80, 2081–2085, 1999.
- Stevens, M. H., R. R. Conway, C. R. Englert, M. E. Summers, K. U. Grossmann, and O. A. Gusev, PMCs and the water frost point in the Arctic summer mesosphere, *Geophys. Res. Lett.*, 28, 4449–4452, 2001.
- Summers, M. E., R. R. Conway, C. R. Englert, D. E. Siskind, M. H. Stevens, J. M. Russell III, L. L. Gordley, and M. J. McHugh, Discovery of a water vapor layer in the Arctic summer mesosphere: Implications for polar mesospheric clouds, *Geophys. Res. Lett.*, 28, 3601–3604, 2001.
- Taylor, M. J., M. Gadsden, R. P. Lowe, M. S. Zalcik, and J. Brausch, Mesospheric cloud observations at unusually low latitudes, *J. Atmos. Sol. Terr. Phys.*, 64, 991–999, 2002.
- Thayer, J. P., N. Nielsen, and J. Jacobsen, Noctilucent cloud observations over Greenland by a Rayleigh lidar, *Geophys. Res. Lett.*, 22, 2961–2964, 1995.
- Thayer, J. P., M. Rapp, A. J. Gerrard, E. Gudmundsson, and T. J. Kane, Gravity wave influences on Arctic mesospheric clouds as determined by the Sondrestrom, Greenland, Rayleigh lidar, *J. Geophys. Res.*, accepted, 2002.
- Thomas, G. E., Mesospheric clouds and the physics of the mesopause region, *Rev. Geophys.*, 29, 553–575, 1991.
- Thomas, G. E., Recent developments in the study of mesospheric clouds, *Adv. Space Res.*, 14, 101–112, 1994.
- Thomas, G. E., Climatology of polar mesospheric clouds: Interannual variability and implications for long-term trends, *Geophys. Monogr.*, 87, 185–200, 1995.
- Thomas, G. E., Is the polar mesosphere the miner's canary of global change?, *Adv. Space Res.*, 18, 149–158, 1996.
- Thomas, G. E., and J. J. Olivero, The heights of polar mesospheric clouds, *Geophys. Res. Lett.*, 13, 1403–1406, 1986.
- Thomas, G. E., and J. J. Olivero, Climatology of polar mesospheric clouds, 2, Further analysis of Solar Mesosphere Explorer data, *J. Geophys. Res.*, 94, 14,673–14,681, 1989.
- Thomas, G. E., R. D. McPeters, and E. J. Jensen, Satellite observations of polar mesospheric clouds by the Solar Backscattered Ultraviolet Spectral Radiometer: Evidence of a solar cycle dependence, *J. Geophys. Res.*, 96, 927–939, 1991.
- Thomas, L., A. K. P. Marsh, D. P. Wareing, and M. A. Hassan, Lidar observations of ice crystals associated with noctilucent clouds at middle latitudes, *Geophys. Res. Lett.*, 21, 385–388, 1994.
- Turco, R. P., O. B. Toon, R. C. Whitten, R. G. Keesee, and D. Hollenbach, Noctilucent clouds: Simulation studies of their genesis, properties and global influences, *Planet. Space Sci.*, 30, 1147–1181, 1982.
- von Cossart, G., P. Hoffmann, U. von Zahn, P. Keckhut, and A. Hauchecorne, Mid-latitude noctilucent cloud observations by lidar, *Geophys. Res. Lett.*, 23, 2919–2922, 1996.
- von Cossart, G., J. Fiedler, U. von Zahn, G. Hansen, and U.-P. Hoppe, Noctilucent clouds: One- and two-color lidar observations, *Geophys. Res. Lett.*, 24, 1635–1638, 1997.
- von Cossart, G., J. Fiedler, and U. von Zahn, Size distributions of NLC particles as determined from 3-color observations of NLC by ground-based lidar, *Geophys. Res. Lett.*, 26, 1513–1516, 1999.
- von Zahn, U., G. von Cossart, J. Fiedler, and D. Rees, Tidal variations of noctilucent clouds measured at 69°N latitude by groundbased lidar, *Geophys. Res. Lett.*, 25, 1289–1292, 1998.
- Witt, G., The nature of noctilucent clouds, *Space Res.*, 157–169, 1969.
- Woodman, R. F., B. B. Balsley, F. Aquino, L. Flores, E. Vazquez, M. Sarango, M. M. Huaman, and H. Soldi, First observations of polar mesosphere summer echoes in Antarctica, *J. Geophys. Res.*, 104, 22,577–22,590, 1999.

---

X. Chu and C. S. Gardner, Department of Electrical and Computer Engineering, University of Illinois at Urbana-Champaign, 1308 West Main Street, Urbana, IL 61801, USA. (xchu@uiuc.edu; cgardner@uiillinois.edu)

R. G. Roble, High Altitude Observatory, National Center for Atmospheric Research, Box 3000, Boulder, CO 80307, USA. (roble@hao.ucar.edu)